CHARACTERIZATION OF THIN LIQUID FILMS ON SURFACES WITH SMALL SCALE ROUGHNESS BY OPTICAL INTERFEROMETRY

by

Helen Lai

A Thesis

Submitted to the Faculty of Purdue University

In Partial Fulfillment of the Requirements for the degree of

Master of Science in Mechanical Engineering

School of Mechanical Engineering

West Lafayette, Indiana

August 2019

THE PURDUE UNIVERSITY GRADUATE SCHOOL
STATEMENT OF COMMITTEE APPROVAL

Dr. Justin A. Weibel, Co-Chair
School of Mechanical Engineering
Dr. Suresh V. Garimella, Co-Chair
School of Mechanical Engineering
Dr. Amy M. Marconnet
School of Mechanical Engineering

Approved by:

Dr. Jay P. Gore
Head of the Graduate Program

For a better future

ACKNOWLEDGMENTS

This work would not be possible without the support of my professors, friends, family, and labmates. I give thanks to Dr. Weibel and Dr. Garimella for making time to discuss any concerns and provide insightful feedback. I appreciate the ideas they've shared with me in the research process and their words of wisdom through unfamiliar territory. I would also like to thank my parents, Suann and Chan Pyng for their loving support and being ever a source of everyday knowledge.

I would like to thank my research group labmates for fostering a positive and supportive atmosphere in the office and lab, being an open forum for research work and casual chatter alike. In particular, I would like to thank Han Hu for his patience teaching me the background for thin liquid film evaporation work and responsiveness when consulted for advice. I would like to thank Monojit Chakraborty for sharing his expertise on the interferometry technique for thin films, as well as Martina Tomelleri for her help in fabricating the experimental facility and collecting the dataset to develop the silicon wafer cleaning process.

Last but not least, I acknowledge the financial support provided by the Purdue's NEPTUNE Center for Power and Energy, funded by the Office of Naval Research under Award Number N000141613109. I am thankful for the support throughout my studies and to everyone I wish only the best.

TABLE OF CONTENTS

LIST OF TABLES

LIST OF FIGURES

NOMENCLATURE

κ	curvature
σ	surface tension
Π	disjoining pressure
δ	film thickness
P	pressure
φ	potential energy
r	radial distance between atoms
A	Hamaker constant
λ	light wavelength
n	refractive index
R	radius of curvature

Subscripts

s	solid
l	liquid
v	vapor

ABSTRACT

Author: Lai, Helen, A. MSME
Institution: Purdue University
Degree Received: August 2019
Title: Characterization of Thin Liquid Films on Surfaces with Small Scale Roughness by Optical Interferometry
Committee Chair: Justin A. Weibel and Suresh V. Garimella

Two-phase heat transfer techniques such a boiling make use of the high latent heat of fluids to enable dissipation of higher heat fluxes from surfaces compared to conventional single-phase cooling methods. To meet the increasing heat flux dissipation requirements of high-power electronic devices, modifications to the surface properties and roughness are often considered as a means to enhance two-phase heat transfer processes. Although surface roughness of varying length scales has been observed experimentally to enhance boiling heat transfer performance, the physical mechanisms that govern this improvement are not widely accepted. Correlations can be developed to map the behavior of specific surface structure geometries, but a broader investigation of the fundamental forces affecting evaporation at the three-phase contact line, which is critically important to the two-phase heat transfer process, may provide more widely applicable insights. In this thesis, an experimental setup was developed to investigate the effect of small scale surface roughness, with feature sizes below 1 micron, on the liquid film profile of a meniscus formed on a surface. This physical film profile can provide insight into how the surface roughness affects disjoining pressure, an important force that affects the phase change heat transfer process at the contact line. Using an interferometry technique to measure the liquid film profile for a model system of octane on silicon substrate with varying roughness, the change in disjoining pressure in the liquid film was observed. We found that the strength of disjoining pressure in the liquid film increases with increasing surface roughness feature depth.

1. INTRODUCTION

1.1 Background

For many years the size of electronic devices has continued to decrease, in part because this scaling of the chip sizes offers benefits including lower resistive power losses and more computing functionality within the same footprint. While providing more computing power in a smaller form factor is desirable for performance in many applications, this size decrease also signifies a considerable increase in density of heat generation. In extreme applications, the concentrated generation of heat at local hotspots can lead to heat fluxes of 1 kW/cm^2, on the same order as the surface of the sun [1]. Dissipation of these highly concentrated hotspots is important to maintaining device temperatures below their functional limits. Because device lifetime is often proportional to the operating temperature of the device, higher operating temperatures reduce the device's time to failure. Such thermal challenges can prevent the adoption of new technologies if system reliability targets are not met. In some applications such as radar electronics, interpretation of the electrical signals are also affected by temperature [2], such that the thermal management approach is directly coupled to performance. As such, thermal management of these devices is becoming a major limiting barrier to continued miniaturization and power increases.

One potential method to manage extremely high heat fluxes is the use of two-phase cooling, i.e., boiling of a coolant that is passed through a heat sink or directly over the device. Two-phase cooling leverages the high latent heat of the working fluid to effectively dissipate heat. Compared to single-phase cooling approaches, boiling offers improved temperature uniformity, owing to the isothermal phase change process, and the capability to dissipate higher heat fluxes at a lower surface superheat. Two-phase heat transfer is known to be enhanced by adding roughness or surface structures to the heated surface. There are multiple mechanisms by which the surface structures can impact the heat transfer performance. These mechanisms include an increase in surface area from the addition of surface structures, surface wettability effects on bubble growth, and enhanced nucleation by specific geometries such as re-entrant cavities. In addition, the complex boiling process has multiple regimes where different physics may govern the vapor generation process. As such, it is difficult to isolate the specific

mechanism by which surface roughness impacts boiling because it affects a system of interdependent physical processes observed as a whole. Experimental correlations have been developed for particular surface geometries, but are generally not applicable outside the boundaries of the respective datasets [3], [4].

To study the one potential effect of surface roughness on the two-phase heat transfer process, without limiting the results to specific surface geometry, we are interested in understanding how roughness affects the fundamental forces involved in the underlying evaporation process. From this understanding of these fundamental forces, it may be possible to build representative models and use them to investigate the effect of particular surface features. We focus on a better understanding of how surface roughness affects the relevant fundamental forces and physical system during the phase change heat transfer process in a very small region at the corner of a nucleated bubble on the heater surface, called the three-phase contact line.

The three-phase contact line is the intersection of the vapor phase in the bubble, the liquid phase in the bulk fluid, and solid phase of the heater surface, for example at the edge of a nucleated vapor bubble (Fig. 1). Zooming in to the scale of microns, the contact “line” region can be represented by three sub-regions: (1) an adsorbed film region where there exists a thin, constant-thickness liquid film, (2) a bulk meniscus region where the liquid-vapor interface curvature tends towards that of the macroscopic bubble, and (3) a transition region between the adsorbed film and bulk meniscus regions. Key physical phenomena in this contact line region are a pressure gradient driven liquid flow from the bulk fluid into the contact line region, strong evaporation at the vapor-liquid interface in the transition region, and conduction heat transfer through the thin liquid film from the surface to the vapor-liquid interface. In this system, no evaporation occurs in the adsorbed film region due to strong attractive molecular forces between the liquid film and solid heater surface. Because of the low conduction resistance through the thin liquid film, most of the phase change heat transfer occurs in the transition region. The evaporation flux has a maximum within the transition region and decreases towards the adsorbed film region, where stronger atomic attractive forces hold liquid atoms to the solid surface. Likewise, the evaporation flux decrease from the maximum towards the bulk meniscus region, as an increasing liquid film thickness imposes a larger conduction resistance.

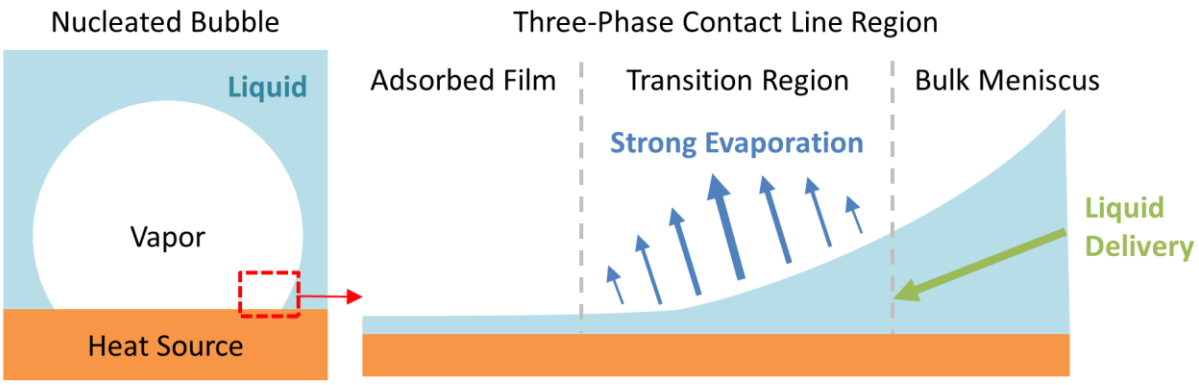

Figure 1. Location of the three-phase contact line for a nucleated bubble and key physical features in the three-phase contact line region.

The total rate of phase change heat transfer in the contact line region at steady state is determined by the pressure balance in this physical system. The pressure in the thin liquid film is the key physical property in this interdependent system. The pressure gradient draws the liquid into the transition region and plays a role in defining the thickness profile of the thin liquid film. This thickness profile then determines the conduction resistance to the vapor-liquid interface, as well as the flow resistance for the liquid being drawn into the transition region. To understand the behavior of this system, consider the components of the liquid pressure, namely the capillary pressure due to the curvature of the vapor-liquid interface and the disjoining pressure from molecular attractive forces. This can be represented by the extended Young-Laplace equation (1).

$$\kappa\sigma_{\mathrm{l}} + \Pi\left(\delta\right) = P_{\mathrm{v}} - P_{\mathrm{l}} \tag{1}$$

The capillary pressure contribution can be captured by measurement or modeling of the thin liquid film profile, from which the curvature can be calculated. Disjoining pressure arises from the attractive force between individual atoms, which can be modeled by the Lennard-Jones potential (Fig. 2). The potential φ is a function of the distance between the atoms r and induces the force felt by the atoms. The two atoms tend towards a separation distance with the lowest potential, such that a positive change in potential is felt as an attractive force. When the change in potential is negative, the force is repulsive. The potential curve predicts that atomic forces between two atoms to be strongly repulsive when very close. Moving the atoms further away from each other, the force becomes strongly attractive at moderate distances and then weakly

attractive the distance between atoms further increases. For thin liquid films, the individual attractive forces felt by the liquid atoms in the film add up to a net attractive force affecting the bulk of the liquid. This net attractive force can be represented as a negative pressure known as the disjoining pressure.

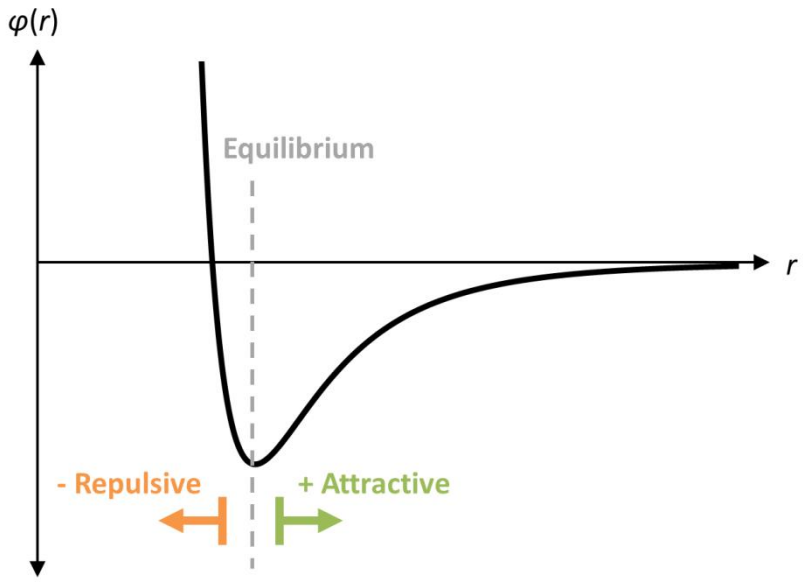

Figure 2. Lennard-Jones potential between two atoms.

Considering only van der Waals interactions, disjoining pressure can be represented by equation (2).

$$\Pi(\delta) = \frac{A}{6\pi\delta^3} \tag{2}$$

The Hamaker constant A accounts for variance in atomic attractive forces between the different fluid and solid atoms. Because disjoining pressure arises from atomic-level forces, it is a function of film thickness, being stronger for thin films where atomic separations are in the strongly attractive region of the Lennard-Jones potential curve and weaker for thick films. Also, the disjoining pressure is expected to be dependent on the spatial distribution of solid atoms relative to the liquid film, such that the surface geometry (such as surface structures or roughness) will affect disjoining pressure strength.

Normally, disjoining pressure can be neglected for liquid films greater than 1 micron because its effect is small [5]. For thin liquid films, this disjoining pressure contributes strongly

to the liquid pressure, and thus the liquid film profile. Understanding this disjoining pressure as a function of film thickness and surface roughness can help improve prediction of the liquid film profile at the contact line. By investigating how this system responds to surface roughness, it may be possible to gain an improved understanding of how surface features affect macroscopic heat transfer behavior.

1.2 Literature Survey

Disjoining pressure plays an important role in the contact line region, although the small force applied makes it difficult to directly measure. A thin liquid film of less than a micron in thickness is too small for a macroscopic pressure probe, and therefore, previous experimental approaches typically infer the disjoining pressure from liquid film thickness measurements. Current techniques for measuring the film profile in thin liquid films are: interferometry [5], [6], reflectometry [7]–[9], ellipsometry [5], [10]–[12], tapping-mode atomic force microscopy (AFM) [13]–[15], non-contact AFM [16], [17], and fluorescence microscopy [18]–[20].

Interferometry measures the change in film thickness between two points, and so it can only capture non-uniform liquid film profiles [21] (Fig. 3). The measurement technique relies on light waves perpendicular to the solid surface with a thin liquid film. Light reflects from the two interfaces, at the solid-liquid interface and the liquid-air interface. Light interference occurs between the two reflected light waves; across a non-uniform thickness liquid film, this leads to a pattern of light and dark fringes corresponding to constructive and destructive interference. The change in film thickness between a dark fringe and the adjacent light fringe is a function of the light wavelength. The spacing between light and dark fringes can thereby be used to calculate the relative change in film thickness between points. This allows measurement of the film profile, but not the absolute thickness of the film. To achieve an absolute film thickness profile, interferometry must be used with another measurement technique. The main limitation of interferometry is that light interference fringes must be clearly observable. The liquid film must also be relatively thin because thicker liquid films can fully absorb the light waves reflecting from the solid-liquid interface. Interferometry can measure liquid films of thickness 90 nm to 1 μm with a vertical resolution of 100 to 200 nm [5]. It offers high lateral resolution which is defined by the optical magnification and imaging sensor, demonstrated in a previous study at 0.144 μm per pixel [6].

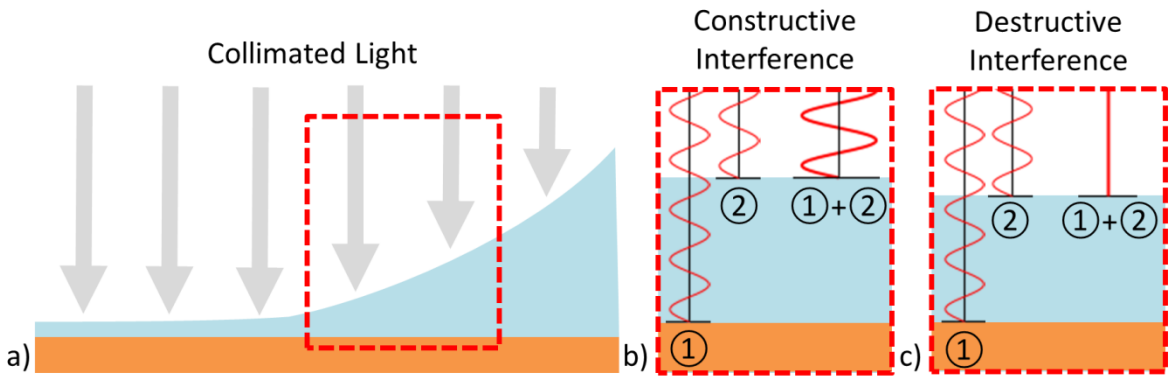

Figure 3. Schematic drawings of light interference for a perpendicular light path through a thin liquid film on a solid surface used in interferometry: a) solid-liquid and liquid-air light reflection interfaces across the imaging area for film profile capture, b) constructive interference that amplifies the light wave, and c) destructive interference.

Reflectometry measures the absolute liquid film thickness at a point [22]. The measurement technique uses a range of light wavelengths at an angle to the solid surface with a thin liquid film. By scanning across a range of light wavelengths, a reflectometer is able to extract an intensity signature as a function of light wavelength. The intensity of the reflected light depends on the phase shift between the light waves reflected at the solid-liquid and liquid-air interfaces, which depends on the film thickness. At a known angle, the wavelengths where the intensity signature reaches maxima and minima represent points where the light waves are in-phase and out-of-phase. This information can be used to determine the film thickness. Reflectometry can be used to measure a steady liquid film profile by scanning across the surface in the lateral direction. The limitation of reflectometry is that it makes an area-averaged measurement of liquid film thickness under the finite spot size of the light beam, which reduces its lateral resolution. For example, a Filmetrics F40-UV microscope-based reflectometer has a measurement area of 16.7 μm × 16.7 μm, though a lateral resolution of 4 μm × 3 μm has been achieved using a modified aperture to change the measurement area [8]. Capturing a liquid film profile with this technique also requires that the liquid film profile be steady an insensitive to movement of the scanning stage. Reflectometry is capable of making a spot measurement of very thin liquid films of thickness 5 to 1000 nm [8].

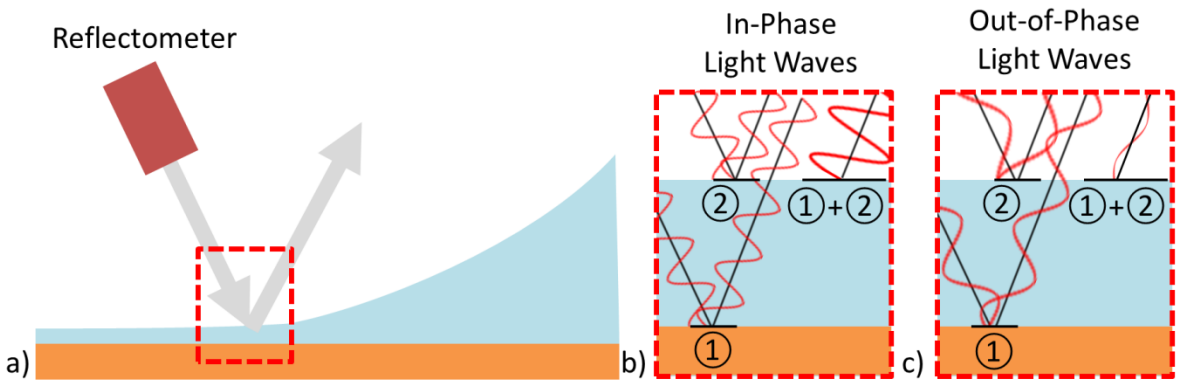

Figure 4. Schematic digrams illustrating the working principles of reflectometry: a) experimental setup showing the angled, single spot light path, b) in-phase waves that increase meausred intensity, and c) out-of-phase waves that decrease measured intensity.

Ellipsometry measures the absolute liquid film thickness at a point [23], [24]. The measurement technique uses polarized light shone at an angle to the solid surface with a thin liquid film (Fig. 5). Like reflectometry and interferometry, light reflected from the solid-liquid and liquid-air interfaces interact and form light interference null points where the two reflections cancel each other out. By changing the polarization of the incident light using the polarizer, multiple null points can be captured for single film thicknesses and used to determine the absolute film thickness. The technique can be used to measure the liquid film profile by scanning across the surface or imaging interference fringes across a surface and extracting null points in 2D. The technique shares limitations with the prior techniques in that the interference null points must be observable, requiring the surface to be somewhat reflective. Ellipsometry is capable of a spot measurement of very thin liquid films from a range of 1 nm to 20 μm with a vertical resolution of 1 to 300 nm [12]. However, the lateral resolution is reduced due to the angled light path used for imaging and area-averaging effects from the finite spot size of the light source. A lateral resolution of 2 μm perpendicular to the light beam and 7.5 μm in line with the light beam has been demonstrated in the literature [23].

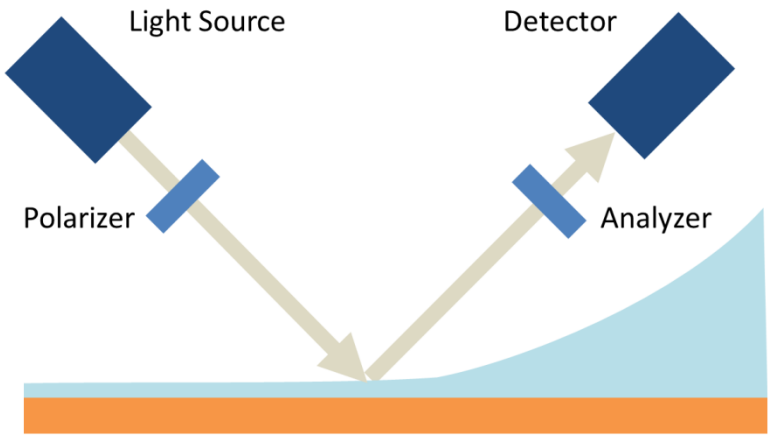

Figure 5. Schematic diagram of the experimental setup requied for ellipsometry showing the angled, single spot light path and typical positions of the polarizer and analyzer.

Tapping-mode atomic force microscopy (AFM) is capable of measuring the liquid pressure and liquid film profile [17]. This technique utilizes a cantilever with a very fine tip that is dipped into and out of contact with the thin liquid film (Fig. 6a). The "lift-off" force required to break the liquid meniscus formed around the cantilever tip when the cantilever is pulled out of contact with the film can be used to calculate the pressure in the liquid film. To measure the liquid film profile, the probe is scanned across the surface using this "lift-off" force to sense the height of the liquid film. The "lift-off" force itself can be used to calculate the pressure in the fluid using a model of the meniscus formed around the probe tip. The main limitation of this technique is that it requires physical contact with the liquid film, which can disturb the system. The lateral resolution is also limited by the cantilever tip size, which has a finite lower limit.

Non-contact AFM can be used to measure the relative liquid film profile [16]. The measurement technique uses a vibrating cantilever in close proximity to the thin liquid film surface (Fig. 6b), but without touching the liquid. The cantilever is affected by attractive Van Der Waals forces that change the amplitude of vibration depending on how close it is from the liquid film surface. The height of the probe is adjusted when scanning across the liquid film surface to maintain the same vibration amplitude, thus keeping the probe at a constant height above the liquid film. The change in probe height represents the change in liquid film profile. The limitation of this technique is that cantilever vibration is very sensitive, so it requires isolation for consistent measurement. This makes the experimental setup more complex. Non-contact AFM is capable of measuring liquid film profiles where the range of film thicknesses

measurable and vertical resolution are limited by the mechanical system used to adjust the probe height, not the liquid film itself. The lateral resolution is limited by the cantilever tip size, demonstrated to be 10 to 15 nm [16].

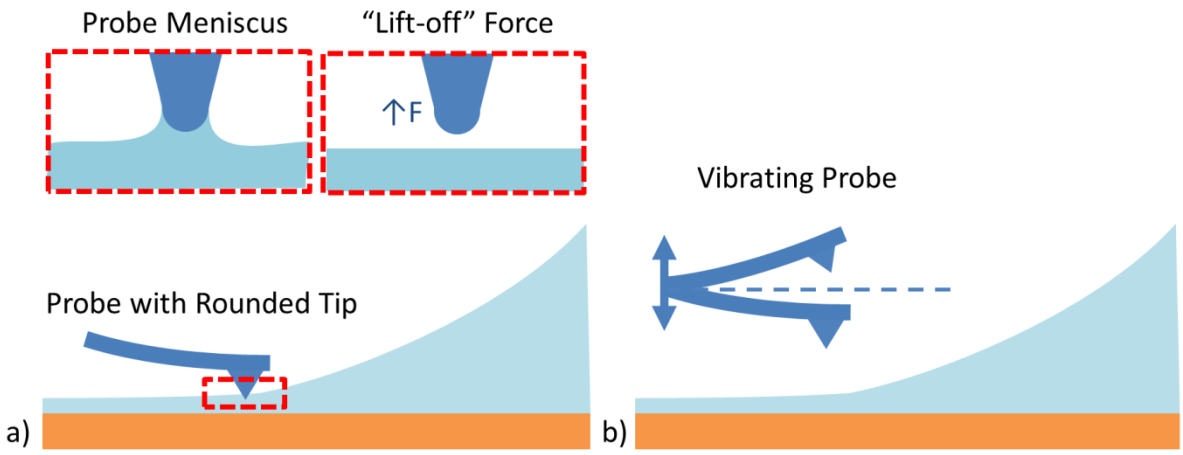

Figure 6. Schematic diagrams of AFM measurement techniques for characterizing liquid films on solid surfaces: a) tapping-mode AFM and b) non-contact AFM.

The last measurement technique described here, fluorescence microscopy, can measure an absolute liquid film thickness profile [25] (Fig. 7). The technique makes use of the addition of two fluorescent dyes to the liquid. By exciting the dye with light, the liquid film re-emission is a function of the volume of liquid and thus the liquid film profile. Normalizing the reemission of the two dyes by each other allows removal of optical non-uniformities and lighting effects. This allows correlation of normalized dye reemission intensity to the liquid film thickness. The limitation of this technique is that the addition of a dye can slightly affect the physical properties of the resulting mixture (e.g., surface tension). It also requires measurement of film thickness by some other technique to generate a correlation between the normalized dye reemission intensity to liquid film thickness. This concept has also been applied to liquid flows using fluorescent seeder particles instead of a dye [26]. The strength of this technique is that once the normalized dye reemission intensity is calibrated as a function of the liquid film thickness, calculation of an unknown liquid film profile is straightforward. Fluorescence microscopy is also capable of achieving high lateral resolution mainly limited by the camera and optical setup. A lateral resolution of 0.2 μm per pixel has been demonstrated in the literature [25].

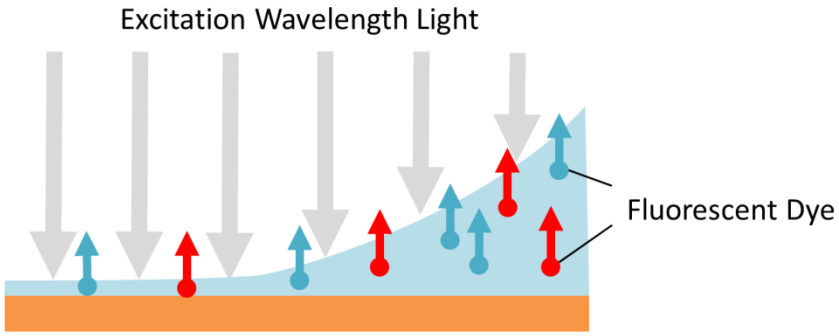

Figure 7. Schematic diagram showing a fluorescence microscopy based technique for characterization of thin liquid films.

1.3 Experimental Objective and Rationale

The objective of this work is to develop an experimental facility to investigate the effect of small scale surface roughness on the liquid film profile, and thereby disjoining pressure, formed on rough surfaces. To indirectly determine the disjoining pressure, we use a model system with controlled evaporation conditions. While this model system is not the exact same as during boiling heat transfer, the trends in the key fundamental forces with surface roughness, namely the disjoining pressure, will hold for all systems.

At equilibrium, we expect the pressure in the liquid film to be constant throughout the liquid film profile. This means that the pressure in the liquid film is the same in the bulk meniscus region as in the adsorbed film region. To make observations about the disjoining pressure in the adsorbed film region, we represent the constant liquid pressure using the extended Young-Laplace equation (1). While the total liquid pressure will remain a constant across the film, the two components of the capillary pressure and disjoining pressure can vary across the liquid film profile. We make two simplifying assumptions from a physical understanding of these component forces at equilibrium. In the adsorbed film region, the liquid film is very flat, i.e., the liquid-air interface has a very low curvature. This means that the capillary pressure, which is defined by the curvature of the liquid-air interface, is also very low and can be neglected in the adsorbed film region. In the bulk meniscus region, the liquid film is considered to be very thick, such that the strength of molecular attractive forces between the liquid and solid atoms, and thus the disjoining pressure, is negligible. Making these simplifying assumptions, the remaining terms in the extended Young-Laplace equation are the disjoining pressure in the adsorbed film region and the capillary pressure in the bulk meniscus region. Therefore, at

equilibrium, the capillary pressure in the bulk meniscus region is equal to the disjoining pressure in the adsorbed film region. By directly measuring the change in liquid film profile curvature as a function of the surface properties, and thus the change in capillary pressure in the bulk meniscus region, we can draw conclusions about the strength of the disjoining pressure in the adsorbed film region.

Using a model system at equilibrium, an experimental setup is used to measure the liquid film profile in the bulk meniscus region, as a means to investigate disjoining pressure in the adsorbed film region. Thus, the experimental target for this study is to measure the liquid film profile close to the contact line for a given liquid and solid combination. The method chosen for achieving this is interferometry because the measurement technique best fulfills experimental requirements. The main experimental requirement is that the measurement technique should be compatible with small scale (below 1 micron) surface roughness that is expected to have an effect on disjoining pressure [27]. The measurement must also be performed remotely through a glass window for a closed system and have the capability to measure the bulk meniscus liquid film profile with enough lateral resolution to calculate the curvature. This closed chamber requirement makes the use of AFM techniques impractical, as incorporating a probe within a closed chamber with small form factor introduces many challenges.

Fluorescence microscopy is also not considered because knowing the material properties of the liquid, namely the surface tension, is important to calculation of the capillary pressure from the liquid film profile. Of the remaining optical measurement techniques, interferometry stands out because it can capture the desired liquid film profile in a single image. Reflectometry and ellipsometry are spot measurements that require a scanning stage to build a liquid film profile. Interferometry fulfills our remote measurement requirement as it can be applied within the working distance of the microscope objective used. With proper selection of microscope objectives, interferometry can be applied to a liquid film inside a chamber through a glass window for imaging. Interferometry is also capable of capturing the liquid film profile at a high lateral resolution primarily limited by the imaging camera, which can measure the liquid film profile at sufficient resolution to perform curvature calculations. Lastly, interferometry for thin liquid films can work with surfaces with rough surfaces so long as the surface is reflective enough to form the desired light interference fringes.

Previous work in the literature using interferometry has demonstrated the ability to measure thin liquid film profiles on a rough transparent surface [21]. This prior work differs from our current study because the experimental setup has an inverted setup where the liquid film profile is upside down and the surface roughness features fabricated on the glass window of the experimental chamber. In this previous study, the authors found that thin liquid film profile is steeper for a smooth surface and flatter for rough surfaces [21]. They observed that adsorbed film thickness increased with increasing roughness. From the thin liquid film profiles, they were able to calculate the evaporative heat transfer from the transition region of the contact line and demonstrate that evaporative heat transfer is enhanced by surface roughness. This study expands upon the previous work in the literature exploring a different solid-liquid combination, enabled by the capability to probe an opaque substrate in the newly developed experimental facility.

2. EXPERIMENTAL APPROACH

2.1 Experimental Facility

The experimental facility was designed to provide a closed chamber and controlled environment while allowing optical access for interferometry, similar in design to the facility used by Chakraborty et al. [28]. The chamber was designed to accommodate the solid-liquid combination of silicon-octane, which was chosen for surface fabrication and wettability reasons. Silicon provides a platform for fabrication of small scale surface roughness using any number of different standard microfabrication processes. The range of available fabrication techniques developed in the literature allowed selection of a relevant fabrication technique for surface structures at the desired length scale of below 1 micron. The fluid, octane, was chosen as because it is a highly wetting fluid which forms the desired three-phase contact line on silicon. This solid-liquid combination has also been used in previous studies in the literature [5], [7], allowing for direct comparison.

The chamber is composed of four primary components (Fig. 8): (1) a circular stainless steel base plate with an inset to accommodate a 2 inch silicon wafer, (2) an O-ring for sealing to the silicon wafer, (3) a Teflon spacer with a micro-hole for fluid charging using a syringe tip, and (4) a stainless steel cover plate with a glass window to allow optical access. The stainless steel cover plate, base plate, and Teflon spacer were custom machined from stock material. The stainless steel base plate has an inset to accommodate the 2 inch silicon wafer substrate. It also has two dowel pins press fit in to ensure proper alignment of the Teflon spacer and stainless steel cover plate when assembled. The Teflon spacer has an inset to align and compress the rubber O-ring around the edge of the silicon wafer, as well as a 0.5 mm diameter micro-hole on one side to allow the chamber to be charged with fluid using a syringe. The bottom of the stainless steel cover has been machined to accommodate the glass window, which is attached using Seal-All, an adhesive that is resistant to organic solvents such as octane. The stainless steel cover plate, base plate, and Teflon spacer all have six through holes for screws to compress the assembled chamber for proper sealing. The silicon wafer used was (100) orientation, 320-340μm thickness,

p-type, 2 inch in diameter, and had a polished surface finish. A list of parts can be found in Appendix A and dimensioned design drawings of the chamber can be found in Appendix B.

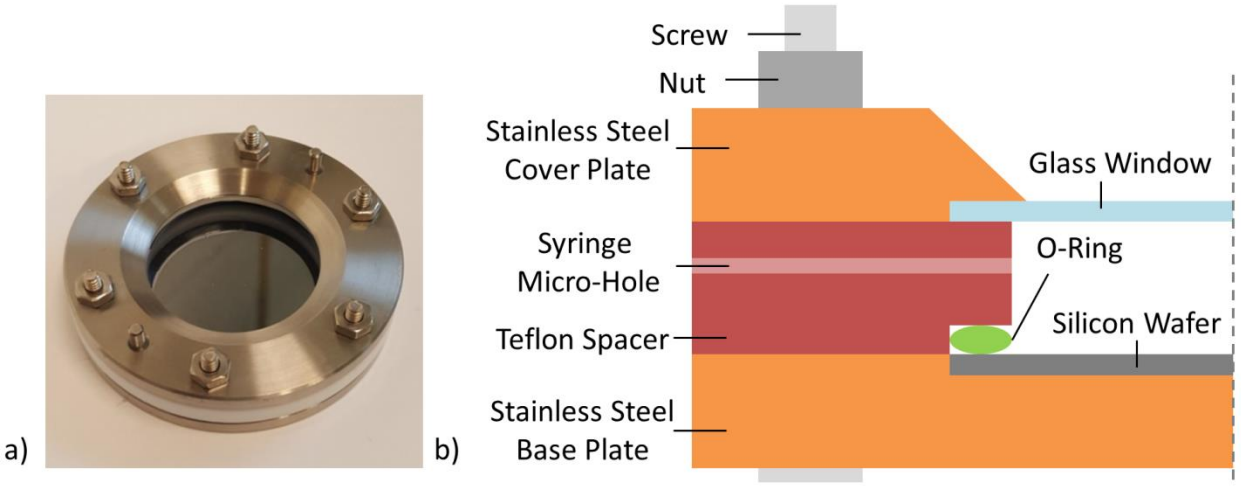

Figure 8. Experimental chamber assembly a) photograph and b) cross-section schematic drawing.

To achieve the desired three-phase contact line feature, the assembled chamber is charged with on the order of 1 to 2 mL of octane and tilted slightly at an angle θ of 2.6° to form a pool on one side of the silicon wafer (Fig. 9). The contact line region of interest in is formed at the edge of the pool, in view of the microscope objective through the viewing window. The microscope used in this study is Olympus BX53M with an Olympus SC50 camera mounted to the microscope for imaging. A green filter accessory was used to filter the light source to monochromatic light at 545-555 nm wavelength. Multiple images along the contact line region were taken using the Olympus LMPlanFI 5x and 10x objectives for the microscope, which have working distances of 22.5mm and 10mm respectively.

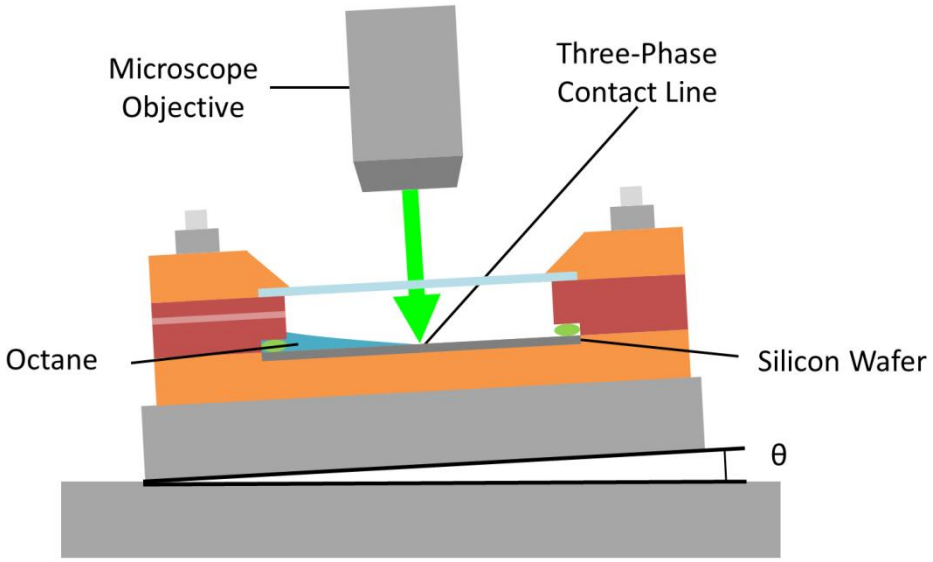

Figure 9. Schematic diagram of the tilted experimental chamber assembly, the three phase contact line formed by tilting the chamber, and imaging microscope objective.

2.2 Experimental Procedure

The target of the experimental work is to capture images of interference fringes in the contact line region. The chamber is first physically assembled starting from the aluminum base plate. The silicon wafer with desired surface properties is placed in the inset and the O-ring is placed on top such that it is centered on the wafer. The Teflon spacer has a groove to accommodate and align the O-ring. The Teflon spacer is placed on top of the O-ring and silicon wafer with the grooved side facing down. Lastly, the aluminum cover plate with glass window closes the top. All plates are aligned by two alignment pins pressed into the base plate using their respective alignment holes in the Teflon spacer and cover plate. The components are held together with six evenly spaced screws which are threaded through and tightened after. Tightening is completed in a star pattern so even pressure is applied to the silicon wafer to avoid wafer breakage.

After assembly, the chamber is partially charged with 1 to 2 mL of octane through a micro-hole in the Teflon spacer using a syringe. The hole is covered with a piece of rubber to reduce leakage after charging. The sealed chamber is then placed on the microscope stage at a tiled angle of 2.6° and allowed to remain undisturbed for at least 6 hours to achieve equilibrium with ambient conditions. This allows the liquid film to settle into a constant position and steady state.

On a clean and smooth surface, this forms parallel interference fringes when viewed under monochromatic light.

2.3 Silicon Wafer Cleaning

To ensure a clean silicon wafer and standardize the data collection processes to ensure consistent data between multiple repeated trials, the experimental setup was used to measure interference fringes formed on a smooth silicon substrate.

One of the major challenges with capturing clear interference fringes is dust particles, which have a size on the same order of magnitude as the liquid film thickness in the contact line region. To perform the experiments, it is critical that the silicon wafer is kept in a clean container and any transfer processes are completed quickly. A cleaning process was also developed to reduce dust within the experimental setup between tests. After cleaning, unperturbed parallel interference fringes should be observed on a smooth silicon surface. The cleaning processes explored included rinsing and soaking in typical silicon wafers cleaning fluids such as acetone, methanol, and isopropyl alcohol, as well as a more aggressive piranha clean.

The final process developed for cleaning silicon wafers was a series of chemical soaks. For each chemical, the plain silicon wafer was placed in a beaker with enough fluid to cover the wafer completely for 15 minutes in an ultrasonicator. The fluids used in order were acetone, methanol, isopropyl alcohol, and then deionized (DI) water. The silicon wafer was allowed to air dry while angled 80° face down in a closed environment after the last DI water soak. After drying, the silicon wafer was placed in a clean storage case until the next experiment. This cleaning process removed residue adhered to the surface between individual tests. It was confirmed to be effective for several repeated trials for a single silicon wafer, but eventually, enough dirt adhered to the surface that a piranha cleaning process had to be performed to achieve a completely clean silicon wafer. The piranha clean process entails soaking the silicon wafer in a 1:3 solution of H_2O_2:H_2SO_4 for 15 minutes inside a fume hood. The solution components react with each other and remove organic residue from the silicon substrate in the process.

2.4 Interferometry Image Capture

In addition to ensuring that the silicon wafer is clean, it was also important to confirm that the measurement location along the contact line and amount of fluid charged into the chamber do not strongly affect the measured liquid film profile. The amount of fluid charged into the chamber can be described by the apparent fill level of the chamber and the distance along the contact line is represented by numbered positions along its length. In Figure 10, apparent fill levels for 40%, 50%, and 60%, as well as positions along the contact line are drawn.

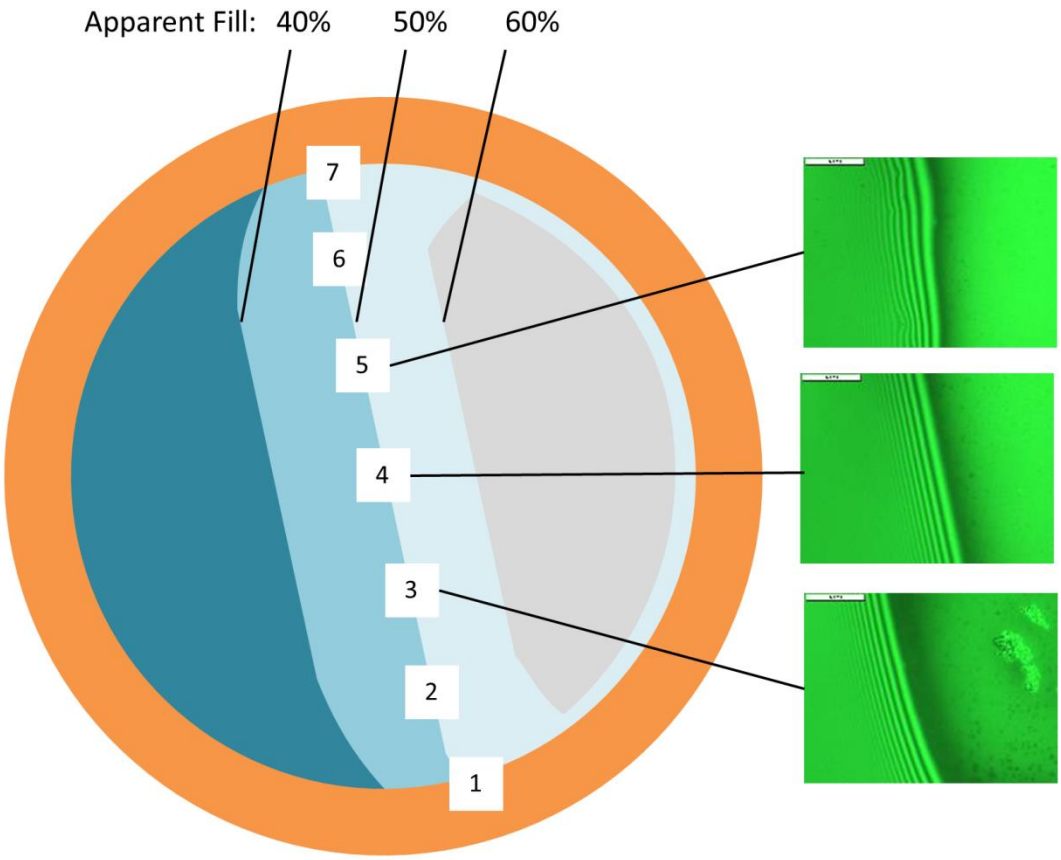

Figure 10. Top-down schematic view of the experimental chamber glass window for 40%, 50%, and 60% apparent fill levels. Positions along the contact line are marked 1 through 7 and corresponding example images captured near the center of the contact line are shown.The white scale bars in these images represents 200 nm.

A large set of interference fringe data was collected for apparent fill levels between 30% and 65%, collecting seven interferometry images along the contact line at each apparent fill level (Fig. 11). For each measured position the chamber is charged to the desired apparent fill level

and allowed to reach equilibrium for at least 6 hours. The average meniscus curvature is extracted from processing the images as described in Chapter 4.1. The plot shows that the average curvature of the liquid film profile is significantly affected near the walls of the chamber, for example at positions 1 and 7. To avoid such edge effects in the chamber, interferometry images of the liquid film profile are taken only close to the center of the wafer between positions 3 and 5, where it remains consistent. Thus, to ensure repeatability between multiple tests, data were collected only for apparent fill levels between 40 and 60% close to the center of the chamber.

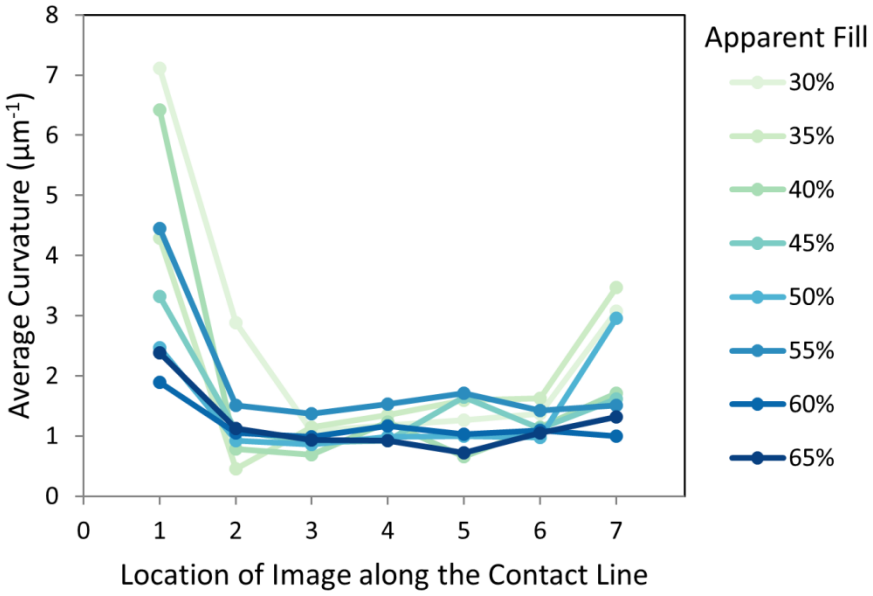

Figure 11. Average curvature of interference fringes captured at different positions along the contact line for various apparent fill levels, as drawn in the schematic in Figure 10.

2.5 Fabrication of Small Scale Roughness

To study how small scale roughness affects the liquid film profile and thus the disjoining pressure, the roughness features must be on the same order of magnitude as the length scale where disjoining pressure is expected to be strong, below 1 μm in height. Fabrication techniques that are capable of creating small scale roughness at this length scale include Ag-catalyzed etching and various plasma etching processes such as deep reactive ion etching (DRIE) [29], [30] and inductively coupled plasma vapor deposition (ICPVD) [31], [32]. For this study, Ag-catalyzed etching was chosen because the fabrication technique was demonstrated to create

roughness features at the scale of 100nm [33]. The fabricated nanowires are stochastic and uniform over the silicon wafer, which is desirable because distinct roughness features will distort the three phase contact line formed on the surface. The length of fabricated nanowires can also be tuned by adjusting the chemical concentrations of the etching solutions or etch time to achieve surfaces with varying levels roughness [34]. The Ag-catalyzed etching process was completed by soaking the wafer in four solutions in sequence [35]. The first solution of 5% HF prepared the silicon wafer, creating H+ terminated surface groups. The second solution of 4.8 M HF and 5 mM $AgNO_3$ deposited silver nanoparticles across the surface. The third solution of 4.8 M HF and 0.4 M H_2O_2 used the deposited silver nanoparticles to etch into the surface, creating nanowire features of greater length with longer etch times. The fourth solution of 1:2 HNO_3:DI water removed the deposited silver nanoparticles. The full recipe is detailed in Appendix C. The resulting roughness features were nanowires fabricated uniformly across the entire wafer, whose height is dependent on etch time. Three surfaces were fabricated with this Ag-catalyzed etching process with the etch times of 20 s, 60 s, and 180 s. After the etch process, the silicon wafers were visually different from a plain silicon wafer, having reduced reflectivity (Fig. 12). To explore the roughness features fabricated on these surfaces, the surface of the silicon wager were imaged near their edges using a JCM-5000 Jeol Table Top scanning electron microscope (SEM) (Fig. 13). The silicon wafer was tilted at 45° to provide the SEM a better view of the surface features to focus the image on. This highly rough edge is visible in Figure 13b and 13c. Left of the edge are roughness features from the thickness of the silicon wafer, a remnant from the manufacturer's growth and slicing process. Right of the edge is the previously polished surface of the silicon wafer that has been fabricated with small scale roughness using the Ag-catalyzed etching process. Comparing the surface features on the right side of each image, the scale of the fabricated nanowires is confirmed to decrease with etch time. The nanowires fabricated on the 180 s etch time surface are on the order of 1 micron. The exact length of the nanowires fabricated on the 60 s and 20 s surfaces are not clearly measureable in the SEMs, but their lengths are significantly below 1 micron and becomes smaller with shorter etch time.

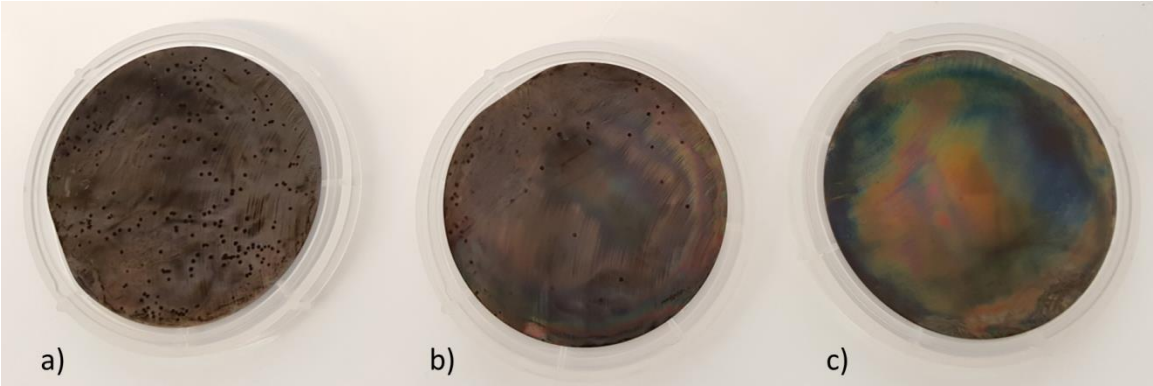

Figure 12. Photograph of the silicon wafers with small scale roughness after the Ag-catalyzed etching process for etch times of a) 180 s, b) 60 s, and c) 20 s.

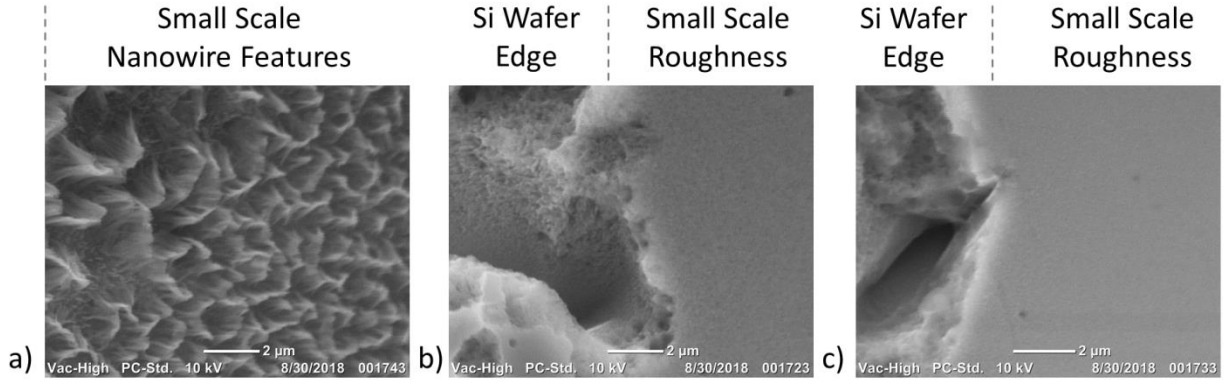

Figure 13. SEM images of the nanowires fabricated on a silicon wafer viewed at a 45° angle for etch times of a) 180 s, b) 60 s, and c) 20 s.

3. DATA PROCESSING

3.1 Liquid Film Profile Calculation using Interferometry

The first steps of the data processing extract a 1D intensity profile for the particular wavelength of light used. This intensity profile captures interference fringes along a path perpendicular to the fringes themselves. The imaging setup was designed to form interference fringes ideal for data processing, which should have two key qualities: (1) each light or dark fringe should have a consistent width, and (2) all fringes should be parallel to each other. Parallel fringes mean the surface is clean of dust that would otherwise distort the interface. An additional step that eases data processing is to align the interference fringes with the x- or y-axis of the image, to ease extracting pixel values in the direction perpendicular to the fringes. Figure 14 shows an example interferometry image of a three phase contact line with some of these ideal qualities for data processing. The left side of the image below the first dark fringe is the adsorbed film region of the contact line. The first couple of light and dark fringes that have varying widths represent the transition region of the contact line where the slope is changing significantly. The thinner, but more consistent light and dark fringes closer to the right side of the image represent the bulk meniscus region of the contact line. The fringes in the bulk meniscus region of the contact line decrease in intensity when moving towards the right side of the image because the film thickness is increasing and absorbing more of the light that must reflect from the solid-liquid interface. The direction perpendicular to the interference fringes in this image is at a slight angle from the x-direction and the desired 1D intensity profile can be extracted by taking a line profile along the white arrow.

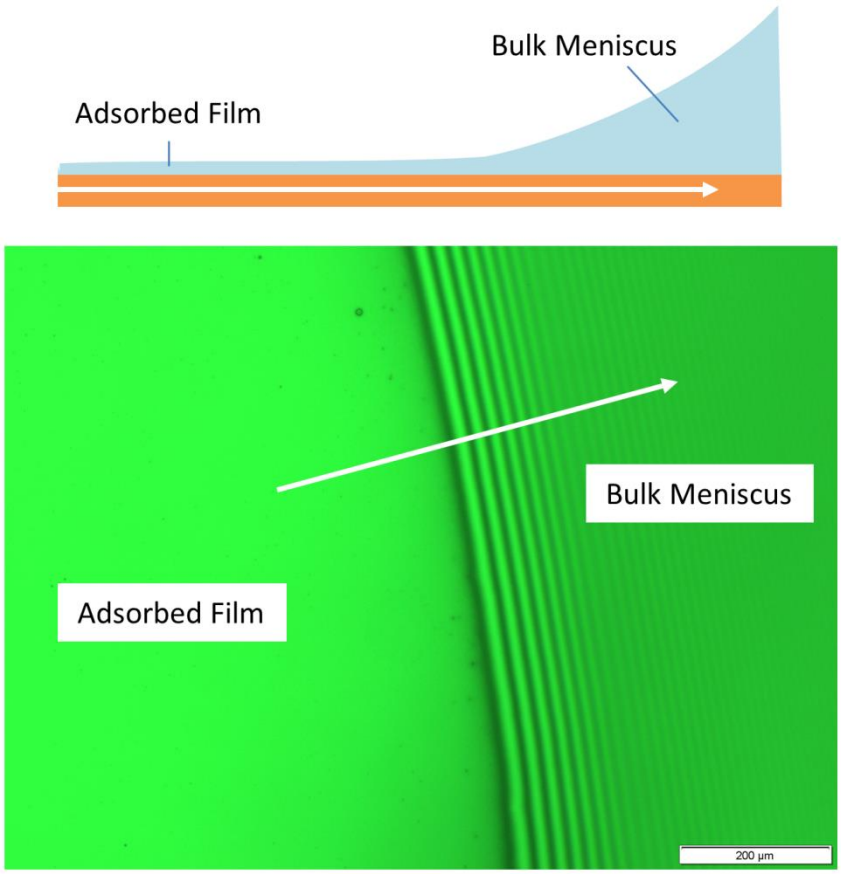

Figure 14. Example of an ideal interferometry image of octane on a smooth silicon surface with consistent width, parallel fringes.

Intermediate steps for converting an interferometry image of octane on a smooth silicon surface to a liquid film profile are shown in Figure 15. To convert the raw image from a three-channel RGB format to intensity, the image is converted to greyscale. Because the light captured by the camera is filtered to green light, the absolute intensity of light is assumed equal to the brightness of the image. This brightness can be obtained from a 0 to 255 scale by converting the image to greyscale. (Fig. 15a)

In this experiment, it was not plausible to align the interference fringes with the x- or y-axis of the camera due to the system requiring at least 6 hours to achieve equilibrium with ambient conditions at its current position. Moving the physical setup to align the fringes would significantly increase the amount of time necessary to complete a test. As such, the images captured have interference fringes at an angle from the x- or y-axes. In the interferometry images captured, the adsorbed film region is on the left side of the image and the bulk meniscus is on the

right side. This required additional processing steps to determine the angle perpendicular to the interference fringes. The full image processing code is provided in Appendix D. Angle calculation starts from a user-drawn line that should be close to perpendicular to the interference fringes. The code uses this user-drawn line as a starting point and performs an angle adjustment by searching a range of angles centered around the input. Figure 15a shows a greyscale image drawn with lines used in the angle determination process: The user drawn line after angle adjustment is drawn in black. The red lines perpendicular to this black line represent the rake of perpendicular profiles used to determine the average standard deviation for angle adjustment. The magenta and cyan lines represent the boundaries of the region considered for intensity profile averaging. At each angle within the searching range, the average standard deviation between a rake of intensity profiles at that angle are compared. Figure 15b shows the average standard deviation between intensity profiles across the range of angles searched. The true angle perpendicular to the fringes is taken as the minimum. As the angle diverges from the true angle in either direction, the standard deviation increases as expected. The 1D intensity profile is obtained by averaging parallel intensity profiles at this final angle across a 400 pixel width. A typical intensity profile is shown in Figure 15c. Before further data processing, the intensity profile is also trimmed to start just before the first valley point and end where the interference fringe data cannot be distinguished from noise.

The intensity profile can now be processed into a liquid film profile by applying a physical model of a thin liquid film on a solid surface. The key to this data processing is identifying peaks and valleys in the intensity profile (Fig. 15c). The change in film thickness between a peak and a neighboring valley is λ/4. We determine this wavelength-dependent constant from the understanding that the change in intensity between a peak and a valley point represents a change in phase shift of λ/2 between the light waves reflected at the solid-liquid and liquid-air interfaces. Compared to the light wave reflected from the liquid-air interface, the light wave reflected from the solid-liquid surface travels an extra distance of twice the film thickness, so a change in film thickness of λ/4 will result in a phase shift of λ/2. The intermediate values between peak and valley points can be calculated by normalizing data points by a minimum window $\bar{G}_{min}$ and maximum window $\bar{G}_{max}$ defined by the peak and valley points. The fitting function for this minimum and maximum window did not change the resulting thin film profile significantly, so the method chosen is a piecewise linear fit between each set of peak or valley points. The

maximum window is plotted in yellow and the minimum window is plotted in green in Figure 15d.

After normalizing the intensity profile by the minimum and maximum windows using equation (3), the relative reflectivity $\bar{G}$ is obtained (Fig. 15e).

$$\bar{G}(x) = \frac{G(x) - G_{min}(x)}{G_{max}(x) - G_{min}(x)} \tag{3}$$

The change in period represents how the change in height varies across the liquid film profile. The peak and valley points are initially more spaced out, signifying the liquid film profile is flatter. The liquid film profile grows steeper as the peak and valley points become closer together near the end of the normalized intensity profile. Note that the dashed line section of the curve in Fig. 15e represents any data points that have been normalized by an extrapolated minimum or maximum window which is necessary for data points before the first fringe in the intensity profile.

This normalized intensity profile can be converted to the liquid film profile using equation (5). This equation comes from the physical understanding that the change in film thickness of λ/4 is represented by a cycle in the interference fringes, which is the distance between one feature to the next feature such as the distance from the first peak to the first valley. Equation (4) defines constants used in equation (5) that are functions of the refractive indices of the solid, liquid, and air phases. The derivation of these equations can be found in the literature [36].

$$r_1 = \frac{n_l - n_v}{n_l + n_v}; \quad r_2 = \frac{n_s - n_l}{n_s + n_l}$$

$$\beta = 2r_1 r_{2;} \quad K = 1 + {r_1}^2 {r_2}^1 \tag{4}$$

$$\delta(x) = \frac{\lambda}{4\pi n_l} \cos^{-1}\left[\frac{\beta + K(1 - 2\bar{G}(x))}{\beta(2\bar{G}(x) - 1 - K)}\right] \tag{5}$$

The final liquid film profile is shown in Figure 15f. The initial portion of the liquid film profile that uses extrapolated minimum and maximum windows is again marked with a dashed line. This extrapolated data is not used in subsequent calculations performed on the liquid film profile.

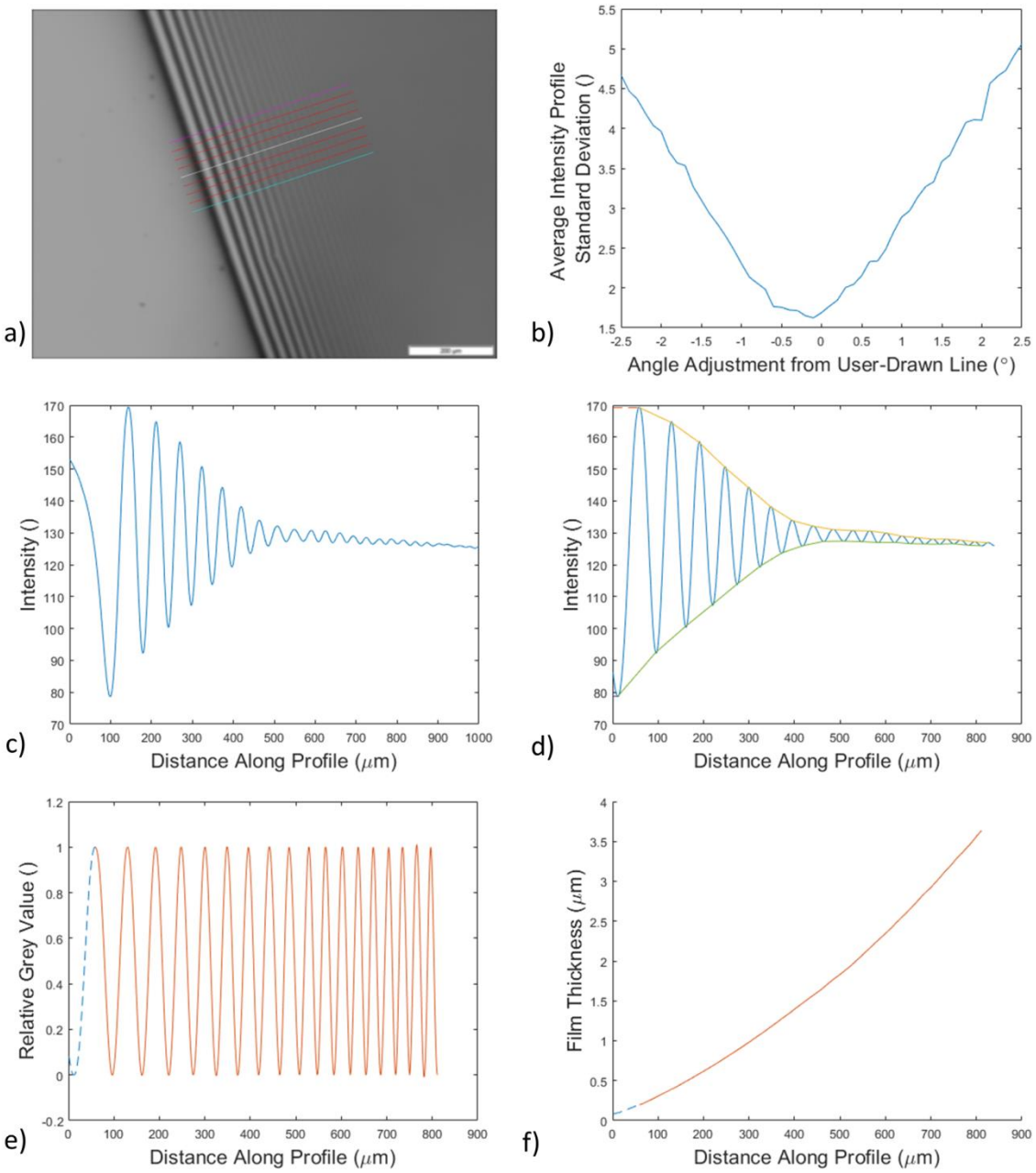

Figure 15. Data processing steps to calculate thin film profile from the raw image: a) user-drawn line overlaid on an interferometry image, b) angle adjustment standard deviation versus searching angle, c) averaged intensity profile, d) min and max window definition, e) intensity profile normalization, and f) thin film profile.

3.2 Frequency Filtering of Surface Roughness

A surface with small scale roughness features introduces random noise into the interferometry image because the camera will capture the roughness as well as the interference fringes formed on top of the surface. To extract the interference fringes from an image with roughness-induced noise, an additional frequency domain filtering step is performed after converting the image to greyscale (Fig. 16a). The image is transformed into the frequency domain using a fast Fourier transform algorithm, which breaks down the image features into representative frequencies. The random roughness-induced noise is expected to be high-frequency noise compared to the pattern of interference fringes because the noise is more spatially dense. To selectively filter out high-frequency noise while retaining the lower frequency interference fringes, a Gaussian low-pass filter is applied. This sets the value of frequencies above a tuned cutoff value to be zero. Performing an inverse Fourier transform to convert the image back from the filtered frequency domain representation results in a smoothed image with reduced noise while leaving the interference fringes relatively unchanged. A frequency filtered image is shown in Figure 16b. To demonstrate the effect of frequency filtering on the subsequent data processing, an intensity profile extracted from the raw image is shown in Figure 16c and an intensity profile after frequency filtering is shown in Figure 16d. The intensity profile from the frequency filtered image has distinguishable peaks and valleys, as well as the sine-wave-like shape expected for an intensity profile of interference fringes. The intensity profile without frequency filtering is difficult to distinguish from the background noise.

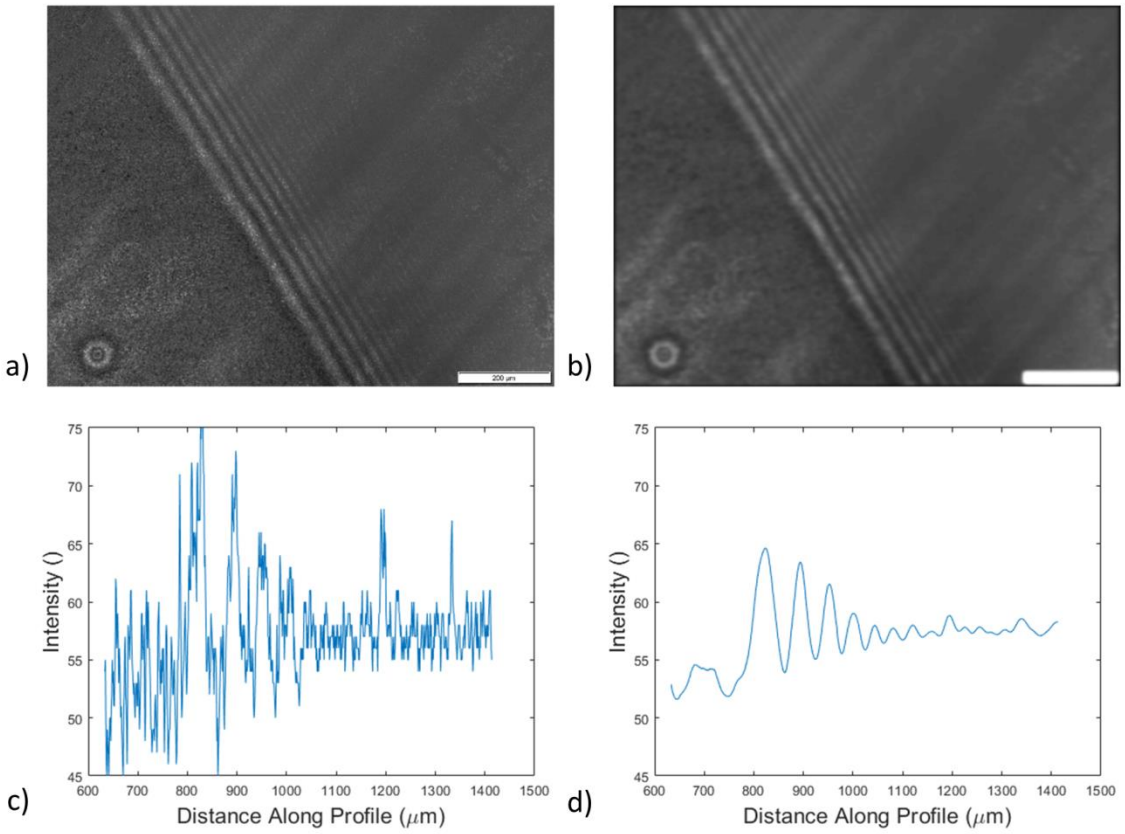

Figure 16. Frequency filtering of interference fringes on the surface with small scale roughness: a) raw image, b) frequency filtered image, c) raw intensity profile, d) frequency filtered intensity profile. The brightness of the raw and frequency filtered images has been increased in this figure for display readability.

4. COMPARISON OF ROUGH SURFACE LIQUID FILM PROFILES

4.1 Liquid Film Profiles on Rough Surfaces

The experimental procedure and data processing steps were performed using the same methodology for four surfaces with varying levels of surface roughness. The liquid film profile positions obtained have an uncertainty equivalent to the lateral resolution, which is set by the resolution of the camera and magnification of the microscope objective. For this experimental setup, the lateral resolution is 0.44 μm per pixel. For the film thickness, the uncertainty can be estimated from observing the change in film thickness induced by shifting any given intensity value by the greyscale resolution of 1 unit. This change in film thickness is dependent on the amplitude of the intensity profile because of the normalization step (Fig. 15e). When the intensity profile is normalized by a larger amplitude, the effect of shifting any given intensity value is decreased. This means the uncertainty is less for the higher amplitude intensity profile close to the adsorbed film region and increases as the amplitude decreases towards the bulk meniscus region. For the example interferometry image used in Figure 15, the change in liquid film profile thickness when shifting the intensity value by 1 ranges from 1.1 nm close to the adsorbed film region up to 66 nm close to the bulk meniscus region where the interference fringes fade out.

The resulting liquid film profiles for a smooth silicon wafer with no surface treatment, as well as surfaces with small scale roughness fabricated using etch times of 20, 60, and 180 s are plotted together in Figure 17. Silicon surfaces with longer etch times have nanowire surface roughness features with greater height. Comparing between the rough surfaces, the liquid film profile has a steeper slope for shorter etch times. The magenta liquid film profiles for the 20 s etched surface have the steepest slope and the green liquid film profiles for the 180 s etched surface have the flattest profiles among the surfaces with roughness features. The liquid film profiles for the 60 s etched surface have a slope between the 20 s and 180 s etched surfaces. These observations align with predictions in the literature for disjoining pressure on rough surfaces, which we expect to manifest in the physical liquid film profile. Specifically, models in the literature predict that disjoining pressure strength increases for surface roughness with increasing depth when features are on the same order of magnitude as the liquid film thickness

[27]. For the roughness features fabricated through the Ag-catalyzed etching process, longer etch times will create nanowires with greater height and thus increased feature depth. Increased disjoining pressure strength will result in a flatter liquid film profile due to the stronger net attractive force between the liquid and solid atoms, which will pull the liquid film to be more conformal to the solid surface. This is the same trend as we observe in the experimental data. The liquid film profile for the 180 s etch time surface has the flattest slope. This physical observation aligns with the expectation that the 180 etch time surface has the strongest disjoining pressure from having small scale roughness features with the greatest depth.

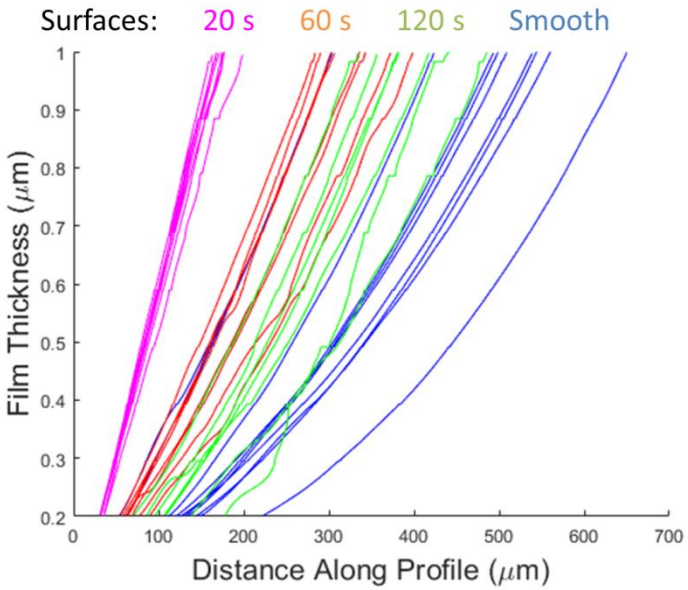

Figure 17. Equilibrium liquid film profiles for octane on smooth and rough silicon surfaces, where the small scale roughness is fabricated by Ag-catalyzed etching with etch times of 20 s, 60 s, and 180 s.

4.2 Disjoining Pressure of Liquid Films on Rough Surfaces

The capillary pressure of the liquid film in the bulk meniscus region can be calculated from the liquid film curvature. The curvature in the bulk meniscus is expected to be a surface-dependent constant along the meniscus because the liquid pressure is constant at equilibrium. The mathematical representation of an interface with constant curvature is a circle. By fitting the expected circle shape to the liquid film profile, the average curvature can be extracted using the definition of curvature in equation (6).

$$\kappa = \frac{1}{R} \tag{6}$$

A least squares method is used to fit a circle to the liquid film profile, as shown for the example case of smooth silicon in Figure 18. This method of curvature calculation works well with experimental data because it is less sensitive to noise in the liquid film profile than local curvature calculations. The mean absolute percent error between the fitted circle and the experimental film profile for each surface is tabulated in Table 1. The lowest mean absolute percent error is 0.4% for the smooth surface, which forms the most ideal interference fringes. The mean absolute percent error increases for surfaces with increasing etch times. The largest mean absolute percent error of 1.3% for the 180 s etched surface is a result of the increased noise in the film profile introduced by the more prominent roughness features.

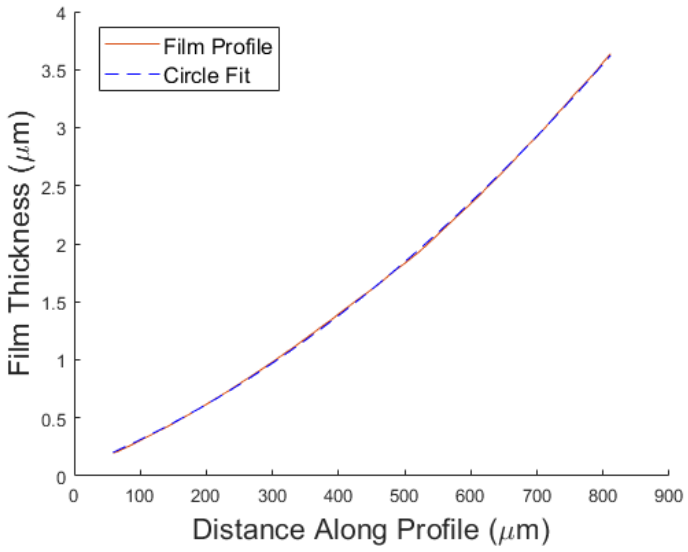

Figure 18. Least squares fit of a circle to the liquid film profile of octane on smooth silicon.

Table 1. Mean absolute percent error between a circle fit by least squares method and the experimentally measured film profile.

Surface	Mean Absolute Percent Error
Smooth	0.4%
20 s Etch	0.5%
60 s Etch	0.6%
180 s Etch	1.3%

The average curvature for each liquid film profile is calculated using this least square fitting method of a circle to the film profile. The average curvature value of octane on smooth silicon found in this study has a median value of 4.9 m^{-1}, which represents a disjoining pressure of 0.1 Pa. This curvature can be compared to a previous study in literature that also measured the liquid film profile of octane on smooth silicon, which found the bulk meniscus curvature value κ to be 63 m^{-1} [5]. The variance in curvature value may be due to the difference in experimental procedure where the previous study has an extra etching step to remove the oxide layer from the silicon wafer before taking measurements. This step changes the surface of the silicon wafer, which can have a strong effect on the disjoining pressure and thus the average curvature of the observed liquid film profile.

The average curvature values for each surface are represented by a box plot to better capture the mean average curvature and range of values (Fig. 19). The box plots show that between the three surfaces with roughness features, the average curvature increases for surfaces with longer etch times. This trend agrees with disjoining pressure predictions from the literature [27] and our observations from the liquid film profiles (Fig. 17). The surfaces with longer etch times and thus increased feature depth have higher average curvature, which represents higher capillary pressure in the bulk meniscus region. At the equilibrium measurement condition, this capillary pressure is equal to the disjoining pressure in the adsorbed film region. Thus, we experimentally observe that disjoining pressure is stronger for surface roughness features with increasing depth.

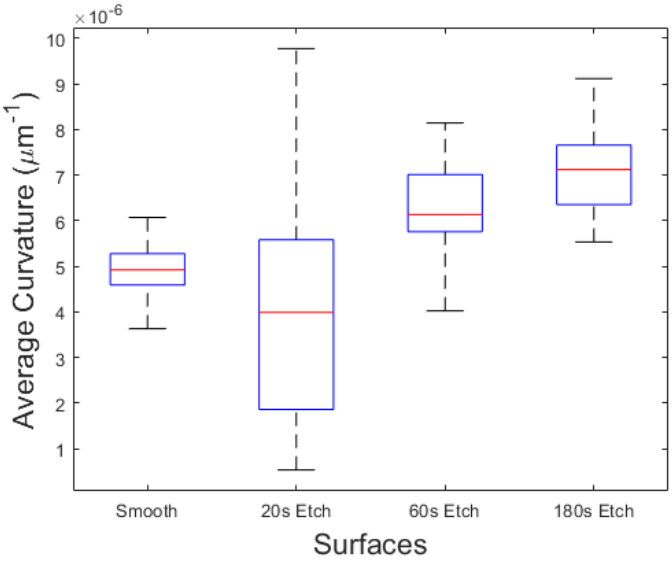

Figure 19. Average curvature of liquid film profiles for octane on smooth and rough silicon surfaces where the small scale roughness is fabricated by Ag-catalyzed etching with etch times of 20 s, 60 s, and 180 s.

5. CONCLUSIONS AND FUTURE WORK

5.1 Conclusions

An experimental facility and procedure were developed to capture a thin liquid film profile on surfaces with small scale roughness. Silicon substrates were fabricated with small scale nanowires features of varying lengths and tested in this facility. Interferometry images for these surfaces with varying roughness were captured and processed to obtain the associated liquid film profiles using a custom image processing code. The liquid film profiles for surfaces with varying roughness were compared and demonstrated the physical trend of liquid film profiles becoming flatter with increasing surface roughness feature depth. At the experimental equilibrium condition, the change in liquid film profile curvature measured in the bulk meniscus region suggests a change in disjoining pressure in the adsorbed film region. The observed trend in liquid film profile slope appears in the calculated average curvature of film profiles and thus the disjoining pressure in the adsorbed film region for each surface. For surfaces with roughness features with increasing depth, we observe that the average curvature of film profiles increases, meaning that disjoining pressure strength also increases.

5.2 Potential Future Work

For a given liquid-solid combination, disjoining pressure in the fluid is a function of the small scale surface roughness features as well as the film thickness of the profile on the surface. This study has made measurements on various rough surfaces for a liquid film profile at a single film thickness, namely, the equilibrium thickness of the adsorbed film at ambient conditions. A potential topic for future work is to measure this adsorbed film thickness and measure disjoining pressure for various film thicknesses on each surface. This can be achieved by designing the experimental chamber to equilibrate at a different temperature that has a different vapor saturation pressure, and thus a different liquid pressure. This change in liquid pressure will allow the measurement of different disjoining pressure and adsorbed film values for the same surface. Building the expected relationship of disjoining pressure as a function of film thickness and surface roughness can provide insight into the relative importance of these variables.

Roughness features can vary in many ways due to the degree of freedom associated with geometries in 3D space. To better understand what qualities of the roughness features are important to the observed disjoining pressure, a potential future work could be to measure disjoining pressure on surfaces with roughness features with more controlled dimensions. Fabricating pillar or groove geometries that are more easily mathematically represented can allow control over roughness properties such as width, length, and feature pitch. It also enables a more direct comparison of experimental results to models in the literature. Building understanding of what qualities of roughness features are important to defining the disjoining pressure of a liquid film on the surface can inform the design of such small scale roughness on heat transfer surfaces.

APPENDIX A. EXPERIMENTAL FACILITY DETAILS

Table 2. Equipment list for the experimental facility

Component	Details
Glass Window	Edmund Optics 50.8 mm Diameter x 1 mm High Efficiency Window
Stainless Steel Stock	McMaster-Carr 303 Stainless Steel Rod 3'' Diameter
Teflon Stock	McMaster-Carr Teflon PTFE Rod 3'' Diameter
Fasteners	18-8 Stainless Steel Hex Drive Flat Head Screws, 6-32 thread, 7/8''Long 18-8 Stainless Steel Hex Nuts, 6-32 thread, 5/16'' Width, 7/64'' Height
Silicon Wafer	University Wafer 2'' Diameter, N Type, P Dopant, <100> Orientation, 300-350 μm Thickness
Syringe	IntelliSpence 50 Gauge 1'' Length Tips Luer Lock Calibrated Manual Syringe
Octane	Sigma Aldrich puriss. p.a., ≥99.0% (GC)
Microscope	Olympus BX53M LMPlanFI 5x, 10x Objectives
Camera	Olympus SC50
Green Light Filter	Nikon Green Interference Filter (GIF) 45 mm Diameter 546/60 nm

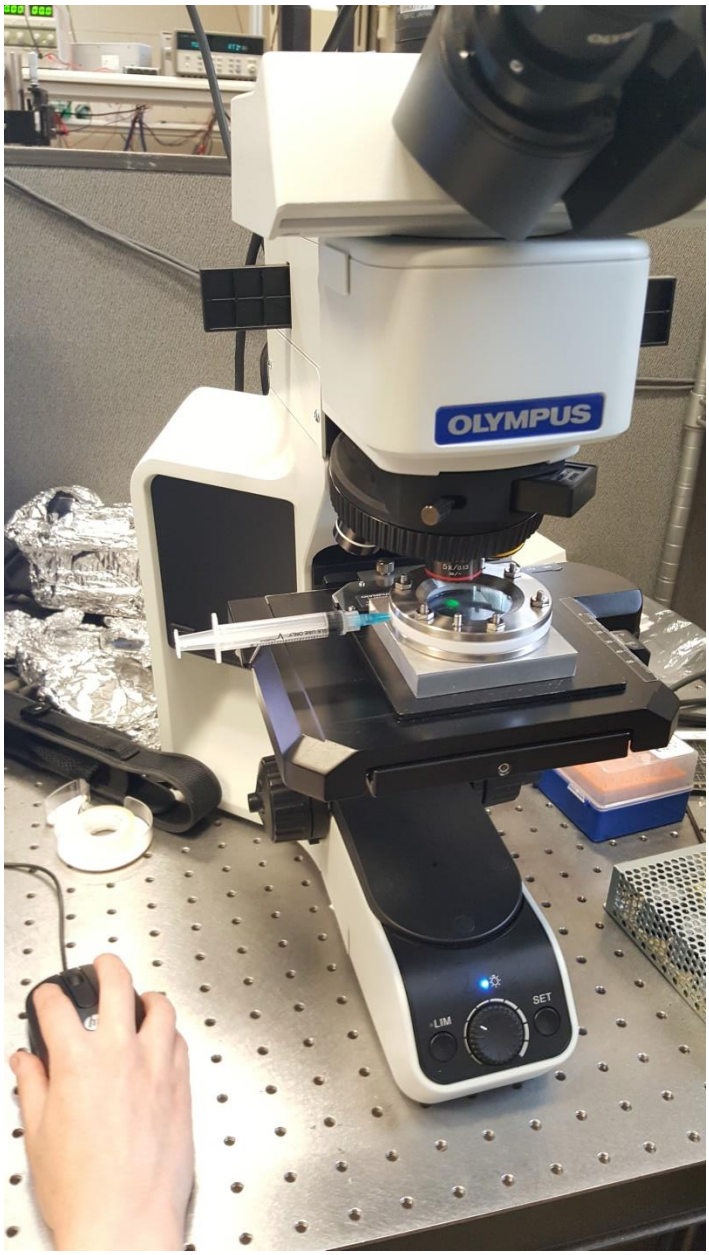

Figure 20. Photo of the experimental facility on a tilted microscope with a syringe used for fluid charging inserted into the micro-hole in the Teflon spacer.

APPENDIX B. MACHINE DRAWINGS OF EXPERIMENTAL FACILITY

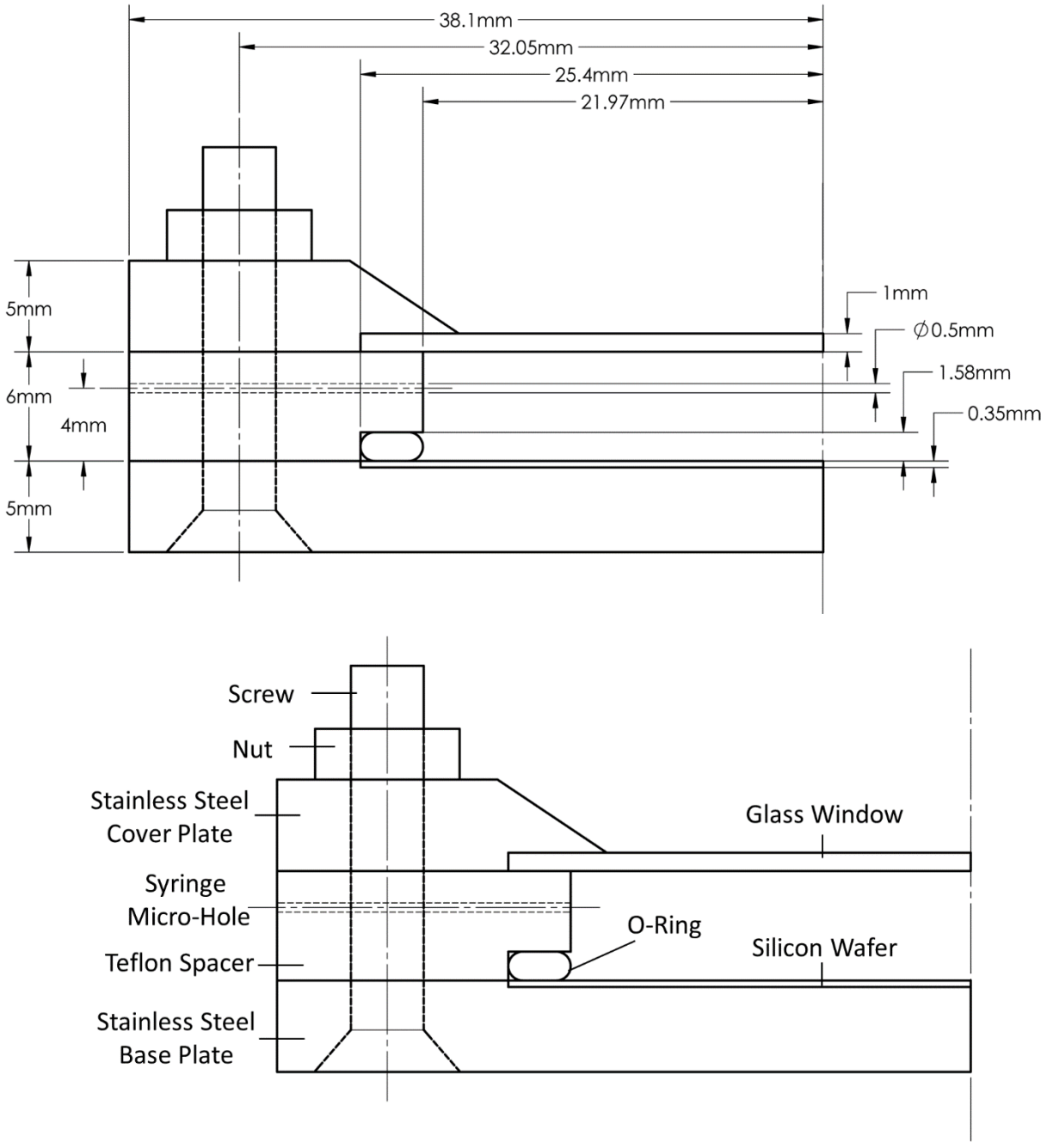

Figure 21. Dimensioned drawings of the experimental facility.

APPENDIX C. AG-CATALYZED ETCHING RECIPE

A chemical etching method was used to fabricate small scale roughness in the form of silicon nanowires uniformly across the surface of a 2-inch silicon wafer. The silicon wafer was first placed in a dipping basket to allow consistent transfer between solutions used in the etching process. The silicon wafer was first soaked in a 5% HF solution for 3 minutes to achieve an H+ terminated surface. After 3 minutes, the wafer was transferred to a large beaker of DI water. This DI water dunk step quickly diluted remnant solution that remained on the silicon wafer after removal from the solution beaker, which stopped the chemicals from acting on the silicon wafer beyond the desired time. This DI water step was used between all solutions. The silicon wafer was then immersed in a 4.8M HF and 5mM $AgNO_3$ solution for 1 minute to deposit Ag nanoparticles on the surface. The wafer was transferred into a fresh beaker of DI water then etched in a 4.8M HF and 0.4M H_2O_2 solution for the desired etch time to create nanowire features. This etch time was varied to achieve surfaces with differing nanowire feature lengths. After being dunked in another fresh beaker of DI water, the silicon wafer was immersed in a 1:2 HNO_3:DI water solution for 30 minutes to dissolve the Ag nanoparticles on the surface. The final result was a silicon wafer with uniform nanowires fabricated across its surface, of which length depended on the etch time in the 4.8M HF and 0.4M H_2O_2 solution.

APPENDIX D. IMAGE PROCESSING CODE

MainCode.m

```
clear all;
close all;
clc;

% Physical constants & setup parameters
%%%%%%%%%%%%%%%%%%%%%%%%%%%%%%%%%%%%%%%%%%%%%%%%%%%%%%%%%%%%%%%%%%%%%%%%%%%%%%%
ns = 1.46; %RI substrate (SiO2)
nl = 1.3989; %RI liquid (Octane)
nv = 1.0; %RI vapor (Air)
lambda = 0.550; %Interferometry light wavelength (micron)
r1 = (nl-nv)/(nl+nv); %liq-vap interface
r2 = (ns-nl)/(ns+nl); %subs-liq interface
kappa = 1+(((r1)^2)*((r2)^2)); %optical parameter
alpha = ((r1)^2)+((r2)^2);
beta = 2*r1*r2;
pixelsize = 200/454; %micrometer/no. pixels for 10x magnification
% pixelsize = 500/572; %micrometer/no. pixels for 5x magnification

%Read in image data and obtain 2D profile
%%%%%%%%%%%%%%%%%%%%%%%%%%%%%%%%%%%%%%%%%%%%%%%%%%%%%%%%%%%%%%%%%%%%%%%%%%%%%%%
imname = 'Purdue_1213';
imrep = 'r2'; %repetition number for multiple test case per image
imtype = '.jpg';
filename = strcat(imname,imtype);
imdat = imread(filename); %read in image data
imgr = rgb2gray(imdat); %convert to greyscale image
imgr2 = imgr;

pq = paddedsize(size(imgr));
threshold = 0.035;
d0 = threshold*pq(1);
h = lpfilter('gaussian', pq(1), pq(2), d0);
f = fft2(double(imgr), size(h,1), size(h,2));
filtered = h.*f;
filteredreal = real(ifft2(filtered));
filteredrealc = filteredreal(1:size(imgr,1), 1:size(imgr,2));
imshow(filteredrealc,[]);

%Call for user to draw line approximately perpendicular to fringes
%%%%%%%%%%%%%%%%%%%%%%%%%%%%%%%%%%%%%%%%%%%%%%%%%%%%%%%%%%%%%%%%%%%%%%%%%%%%%%%
[p_x, p_y, p_all] = improfile; %GUI call for user-defined start/end points to
extract profile (draw line in dir: adsorbed -> bulk + press enter)
xdist = (p_x(end)-p_x(1))*pixelsize; %find physical dist between user-defined
points in x-dir
ydist = (p_y(end)-p_y(1))*pixelsize; %find physical dist between user-defined
points in y-dir
slope = atan(ydist/xdist);
linlength = sqrt(xdist^2 + ydist^2)/pixelsize; %length of line drawn by user
```

```
indexsize = linlength/length(p_all); %find physical dist between profile
indicies: hypotenuse of xdist and ydist divided by total no. points

%Search +/- angle based on user-drawn line to find ideal averaging angle
%%%%%%%%%%%%%%%%%%%%%%%%%%%%%%%%%%%%%%%%%%%%%%%%%%%%%%%%%%%%%%%%%%%%%%%%%%%
drad = 0.1/360*2*pi; %angle increment to check at (delta radians)
radpts = (25*2)+1; %number of points to check @ drad increment
radrange = (1:radpts)-ceil(radpts/2); %adjust range to be +/- centered around
0
avgradius = 200; %length in perpendicular direction to average across
snippingunit = 50; %unit length for spacing of rake of points for std.dev.
calc (to reduce calc time, full set of lines not used until final step)

mismat = mismatchcalc(filteredrealc, p_x, p_y, linlength, avgradius,
snippingunit, (slope + drad*radrange(1))); %calculates avg. std.dev. between
profiles
for j = 2:radpts
    mismat(j) = mismatchcalc(filteredrealc, p_x, p_y, linlength, avgradius,
snippingunit, (slope + drad*radrange(j))); %populate matrix of avg. std.dev.
for range of angles
end
[beststd, bestind] = min(mismat); %find angle with lowest std.dev. (ideal
angle)
bestslope = slope + drad*radrange(bestind); %apply angle adjustment to slope
slope_correction = drad*radrange(bestind)/(2*pi)*360 %print slope correction
to command window

hold on; %maintain greyscale image when plotting lines used in calculation
zsize = avgradius/snippingunit; %number of rake lines needed
for j=1:zsize
    p_xpost = [p_x(1) (p_x(1)+linlength*cos(slope))] +
j*snippingunit*sin(bestslope); %transpose line L/R perpendicularly(rakes)
    p_ypost = [p_y(1) (p_y(1)+linlength*sin(slope))] -
j*snippingunit*cos(bestslope);
    p_xnegt = [p_x(1) (p_x(1)+linlength*cos(slope))] -
j*snippingunit*sin(bestslope);
    p_ynegt = [p_y(1) (p_y(1)+linlength*sin(slope))] +
j*snippingunit*cos(bestslope);
    plot(p_xpost, p_ypost, 'r'); %plot rake lines in red
    plot(p_xnegt, p_ynegt, 'r');
end
p_xpos = [p_x(1) p_x(end)] + avgradius*sin(bestslope); %transpose line L/R
perpendicularly(boundaries in white)
p_ypos = [p_y(1) p_y(end)] - avgradius*cos(bestslope);
p_xneg = [p_x(1) p_x(end)] - avgradius*sin(bestslope);
p_yneg = [p_y(1) p_y(end)] + avgradius*cos(bestslope);
plot(p_x, p_y, 'w');
plot(p_x, p_y, 'w', p_xpos, p_ypos, 'm', p_xneg, p_yneg, 'c');  %plot
centerline and boundary lines

h = figure(1); %save image w/ user-drawn line + rakes + boundaries
pname = strcat(imname, imrep,' 0 BW image boundaries');
saveas(h, pname, 'png');

h = figure(2); %plot + save image w/ standard deviation vs. angle
plot((radrange*0.1), mismat);
```

```
title('Average Intensity Profile Standard Deviation')
xlabel('Angle from User-Drawn Line (\circ)')
ylabel('Average Intensity Profile Standard Deviation ()')
pname = strcat(imname, imrep,' 1 angle adj');
saveas(h, pname, 'png');

%Average profile across perpendicular direction
%%%%%%%%%%%%%%%%%%%%%%%%%%%%%%%%%%%%%%%%%%%%%%%%%%%%%%%%%%%%%%%%%%%%%%%%%%%%%%%
targetlength = size(p_all)-5; %trim all profiles by a tiny bit incase
improfile line calcs are off by a couple pixels
p_avg = p_all(1:targetlength); %trim to target length
for i = 1:avgradius %average all profiles within boundaries
    perp_pos = improfile(filteredrealc, ([p_x(1)
(p_x(1)+linlength*cos(slope))] + i*sin(bestslope)), ([p_y(1)
(p_y(1)+linlength*sin(slope))] - i*cos(bestslope)));
    perp_neg = improfile(filteredrealc, ([p_x(1)
(p_x(1)+linlength*cos(slope))] - i*sin(bestslope)), ([p_y(1)
(p_y(1)+linlength*sin(slope))] + i*cos(bestslope)));
    p_avg = p_avg + perp_pos(1:targetlength) +
perp_neg(1:targetlength); %trim to target length + sum all profiles
end
p_avg = p_avg./(1 + 2*avgradius); %divide by number of profiles to attain
average from sum
[p_x, p_y, p_all] = improfile(filteredrealc, p_xpos, p_ypos); %L boundary
line profile
[p_x2, p_y2, p_all2] = improfile(filteredrealc, p_xneg, p_yneg); %R boundary
line profile

h = figure(5); %plot L/R boundary 1px line profiles + average line profile
across radius avgradius
p_avg = p_all;
plot(find(p_avg), p_avg)
plot(find(p_avg), p_avg, '', find(p_all), p_all, '--', find(p_all2), p_all2,
'--') %plot profile between user-defined points
title('Intensity Profile Along Line')
xlabel('Distance Along Profile (\mum)')
ylabel('Intensity ()')
pname = strcat(imname, imrep,' 2 LCR boundaries');
saveas(h, pname, 'png');

%Truncate data to relevant(user-defined) fringe area
%%%%%%%%%%%%%%%%%%%%%%%%%%%%%%%%%%%%%%%%%%%%%%%%%%%%%%%%%%%%%%%%%%%%%%%%%%%%%%%
[cutoff_x, y] = ginput(2); %GUI call for user-defined start/end points
(adsorbed/first peak -> last distinguishable fringe/bulk noise)
cutoff_x = round(cutoff_x); %round double to integer -> index of desired
truncation points
p_all_trim = p_avg(cutoff_x(1):cutoff_x(2)); %truncate data to two points
selected
p_all_trim_index = find(p_all_trim); %create matrix of indices for trimmed
raw data

%Smooth curve to locate peaks/valleys
%%%%%%%%%%%%%%%%%%%%%%%%%%%%%%%%%%%%%%%%%%%%%%%%%%%%%%%%%%%%%%%%%%%%%%%%%%%%%%%
p_all_trim_smooth = smooth(p_all_trim); %smooth curve once to minimize noise
[pks, locs] = findpeaks(p_all_trim_smooth); %find local maxima of smoothed
curve
```

```
[vals, locs2] = findpeaks((p_all_trim_smooth.*-1)); %find local minima of
smoothed curve by finding local maxima of -1*data
vals = -1*vals; %revert local minima to positive by -1*vals

h = figure(2); %plot smooth vs. raw data, identified min/max points
plot(p_all_trim_index, p_all_trim_smooth, '', locs, pks, 'o k', locs2, vals,
'o c')

smoothenough = input('Smooth enough? (y/n)', 's'); %prompt for user to decide
if peaks/valleys are correctly identified from figure2
while(smoothenough == 'n') %smooth curve until peaks/valleys correctly
identified using findpeaks(...)
    p_all_trim_smooth = smooth(p_all_trim_smooth); %smooth curve again
    [pks, locs] = findpeaks(p_all_trim_smooth); %find local maxima of new
smooth curve
    [vals, locs2] = findpeaks((p_all_trim_smooth.*-1)); %find local minima of
new smooth curve by finding local maxima of -1*data
    vals = -1*vals; %revert local minima to positive by -1*vals

    plot(indexsize*p_all_trim_index, p_all_trim_smooth, '', indexsize*locs,
pks, 'o k', indexsize*locs2, vals, 'o c') %plot re-smoothed vs. raw data,
identified min/max points
    smoothenough = input('Smooth enough? (y/n)', 's'); %prompt again for user
to decide if peaks/valleys are correctly identified from figure2
end
locs_s = locs; %save locations of smoothed peaks for comparison to raw peaks
locs2_s = locs2; %save locations of smoothed valleys for comparison to raw
valleys
title('Intensity Profile Along Line')
xlabel('Distance Along Profile (\mum)')
ylabel('Intensity ()')
pname = strcat(imname, imrep,' 3 smooth pks+vals');
saveas(h, pname, 'png');

%Second trim to set beginning at 10px before first fringe so all profiles
start at same position
%%%%%%%%%%%%%%%%%%%%%%%%%%%%%%%%%%%%%%%%%%%%%%%%%%%%%%%%%%%%%%%%%%%%%%%%%%%
p_all_trim_smooth = p_all_trim_smooth((locs2(1)-10):end); %trim beginning to
be 10 points prior to first fringe
p_all_trim = p_all_trim((locs2(1)-10):end);
[pks, locs] = findpeaks(p_all_trim_smooth); %update all related variables
after second trimming
[vals, locs2] = findpeaks((p_all_trim_smooth.*-1));
vals = -1*vals;
locs_s = locs;
locs2_s = locs2;
p_all_trim_index = find(p_all_trim);

%Extrapolate on adsorbed film side(necessary to set film profile to 0 in
adsorbed layer region)
%%%%%%%%%%%%%%%%%%%%%%%%%%%%%%%%%%%%%%%%%%%%%%%%%%%%%%%%%%%%%%%%%%%%%%%%%%%
vals = [vals(1); vals]; %add temporary point for extrapolation: min window
left of first valley = const.
pks = [pks(1); pks]; %add temporary point for extrapolation: max window left
of first peak = pinned to first point on profile
locs2_s = [1; locs2_s]; %add temporary indices for interpolation
```

```
locs_s = [1; locs_s];
pks3_s = interp1(locs_s, pks, find(p_all_trim_smooth),
'linear'); %interpolate min/max window w/ linear fit between peaks/valleys
vals3_s = interp1(locs2_s, vals, find(p_all_trim_smooth), 'linear');
vals = vals(2:end); %remove temporary point after extrapolation
locs2_s = locs2_s(2:end); %remove temporary index
if(locs_s(end) > locs2_s(end)) %determine if line profile ends in peak or
valley. if end w/ peak
    cutoff_x2_s(2) = locs2_s(end); %trim to last valley
    locs_s = locs_s(1:(end-1)); %trim last peak
else
    cutoff_x2_s(2) = locs_s(end); %if end w/ valley, trim to last peak
    locs2_s = locs2_s(1:(end-1)); %trim last valley
end
pks4_s = pks3_s(1:cutoff_x2_s(2)); %trim min/max envelope to only include
data between known peaks/valleys
vals4_s = vals3_s(1:cutoff_x2_s(2));
p_gr_trim2_s = p_all_trim_smooth(1:cutoff_x2_s(2)); %trim raw data to only
include data between known peaks/valleys
p_gr_trim2_index_s = find(p_gr_trim2_s); %get index for trimmed data

figure(19); %plot raw data and min/max envelope, trimmed to non-extrapolation
points(raw data, linear fit)
plot(indexsize*p_all_trim_index, p_all_trim, '',
indexsize*p_all_trim_index(1:locs_s(2)), pks3_s(1:locs_s(2)), '--',
indexsize*p_all_trim_index(locs_s(2):end), pks3_s(locs_s(2):end), '',
indexsize*p_all_trim_index(1:locs2_s(1)), vals3_s(1:locs2_s(1)), '--',
indexsize*p_all_trim_index(locs2(1):end), vals3_s(locs2_s(1):end), '');
title('Intensity Profile Min/Max(Raw) Linear Fit')
xlabel('Distance Along Profile (\mum)')
ylabel('Intensity ()')

%Calculate film profile from trimmed data
%%%%%%%%%%%%%%%%%%%%%%%%%%%%%%%%%%%%%%%%%%%%%%%%%%%%%%%%%%%%%%%%%%%%%%%%%%%%
delta_s = Raw2Profile(p_gr_trim2_s, locs_s, locs2_s, pks4_s, vals4_s,
indexsize, beta, kappa, lambda, n1, 0); %smooth curve, linear fit min/max
envelope

%Fit a circle to non-extrapolated data using least squares method
%Use function CircleFitByPratt resource from Matlab Website
%%%%%%%%%%%%%%%%%%%%%%%%%%%%%%%%%%%%%%%%%%%%%%%%%%%%%%%%%%%%%%%%%%%%%%%%%%%%
circlefit = CircleFitByPratt( [indexsize*p_gr_trim2_index_s(locs_s(2):end) ,
delta_s(locs_s(2):end)] ); %fit circle to data
curvature = 1/circlefit(3) %curvature = 1/r. circlefit has (centroid x,
centroidy, radius)

cx = indexsize*p_gr_trim2_index_s(locs_s(2):end); %calculate points on fitted
circle for plotting
cy = circlefit(3).*sin( -acos((cx - circlefit(1))./circlefit(3))) +
circlefit(2);

h = figure(11); %plot film profile(smoothed data, linear fit min/max
envelope), peak/valley points, fit circle
hold on;
% plot(indexsize*p_gr_trim2_index_s(locs_s), delta_s(locs_s), 'o',
indexsize*p_gr_trim2_index_s(locs_s), delta_s(locs_s), 'o');
```

```
plot(indexsize*p_gr_trim2_index_s(1:locs_s(2)), delta_s(1:locs_s(2)), '--',
indexsize*p_gr_trim2_index_s(locs_s(2):end), delta_s(locs_s(2):end), '', cx,
cy, '') %smooth curve, linear fit min/max envelope
title('Film Thickness Profile')
xlabel('Distance Along Profile (\mum)')
ylabel('Film Thickness (\mum)')
pname = strcat(imname, imrep,' 4 smooth profile');
saveas(h, pname, 'png');

finalprof_x = indexsize*p_gr_trim2_index_s(locs_s(2):end); %create variables
to extract meniscus profile data -> plotting
finalprof_y = delta_s(locs_s(2):end);

pname = strcat(imname, imrep,' workspace');
save(pname, 'alpha', 'avgradius', 'bestslope', 'beststd', 'beta', 'circlefit',
'curvature', 'cutoff_x', 'cutoff_x2_s', 'cx', 'cy', 'delta_s', 'drad',
'filteredrealc', 'finalprof_x', 'finalprof_y', 'indexsize', 'kappa', 'lambda',
'locs', 'locs2', 'locs2_s', 'locs_s', 'mismat', 'nl', 'ns', 'nv', 'p_all',
'p_all2', 'p_all_trim', 'p_all_trim_index', 'p_all_trim_smooth', 'p_avg',
'p_gr_trim2_index_s', 'p_gr_trim2_s', 'pixelsize', 'pks', 'pks3_s', 'pks4_s',
'r1', 'r2', 'slope', 'slope_correction', 'snippingunit', 'threshold', 'vals',
'vals3_s', 'vals4_s', 'xdist', 'ydist');
```

Raw2Profile.m

```
function [ film_profile ] = Raw2Profile( rawdata, peaklocs, valleylocs,
maxenvelope, minenvelope, indexsize, beta, kappa, lambda, nl, viewplots)
%Interferometry Data to Film Profile
%   Method of trimming, calculating peaks/valleys/min/max envelopes is
variable and user-determined before being fed into this function

datindex = find(rawdata); %create matrix of indices for raw data

%Calculate relative grey value
%%%%%%%%%%%%%%%%%%%%%%%%%%%%%%%%%%%%%%%%%%%%%%%%%%%%%%%%%%%%%%%%%%%%%%%%%%%%
g_rel = (rawdata - minenvelope)./(maxenvelope - minenvelope); %(gval - gmin)
/ (gmax - gmin)
if(viewplots == 1) %plot relative grey value if plots desired
    figure(20);
    plot(indexsize*datindex(1:peaklocs(2)), g_rel(1:peaklocs(2)), '--',
indexsize*datindex(peaklocs(2):end), g_rel(peaklocs(2):end), '')
    title('Relative Grey Value')
    xlabel('Distance Along Profile (\mum)')
    ylabel('Relative Grey Value ()')
end

%Normalize grel values between 0 and 1 by threshold so arcos() in formula
gives proper values
%%%%%%%%%%%%%%%%%%%%%%%%%%%%%%%%%%%%%%%%%%%%%%%%%%%%%%%%%%%%%%%%%%%%%%%%%%%%
for(i = 1:length(g_rel)) %for all data points...
    if(g_rel(i) > 1) %if value is greater than 1, set to 1
        g_rel(i) = 1;
    end
    if(g_rel(i) < 0) %if value is less than 0, set to 0
        g_rel(i) = 0;
```

```
    end
end
if(viewplots == 1) %plot normalized relative grey value if plots desired
    figure(21);
    plot(indexsize*datindex(1:peaklocs(2)), g_rel(1:peaklocs(2)), '--',
indexsize*datindex(peaklocs(2):end), g_rel(peaklocs(2):end), '',
indexsize*peaklocs, g_rel(peaklocs), 'o k', indexsize*valleylocs,
g_rel(valleylocs), 'o k')
    title('Normalized Relative Grey Value')
    xlabel('Distance Along Profile (micrometer)')
    ylabel('Normalized Relative Grey Value ()')
end

%Calculate theta from normalized grel values
%%%%%%%%%%%%%%%%%%%%%%%%%%%%%%%%%%%%%%%%%%%%%%%%%%%%%%%%%%%%%%%%%%%%%%%%%%%%%%%
theta = (1/2)*acos((beta + (kappa*(1-(2*g_rel)))))./((beta*((2*g_rel)-1))-
kappa)); %calculate theta (eq from paper)
if(viewplots == 1) %plot theta if plots desired
    figure(22);
    plot(indexsize*datindex(1:peaklocs(2)), theta(1:peaklocs(2)), '--',
indexsize*datindex(peaklocs(2):end), theta(peaklocs(2):end), '',
indexsize*peaklocs, theta(peaklocs), 'o k', indexsize*valleylocs,
theta(valleylocs), 'o k')
    title('Theta')
    xlabel('Distance Along Profile (micrometer)')
    ylabel('Theta ()')
end

%Calculate delta(film thickness) using periodic formula for positive and
negative slope regions
%%%%%%%%%%%%%%%%%%%%%%%%%%%%%%%%%%%%%%%%%%%%%%%%%%%%%%%%%%%%%%%%%%%%%%%%%%%%%%%
delta = 0.*theta; %create empty matrix to fill
for i = 1:(length(peaklocs)-1) %loop through curve split into 'v' shaped
sections, using the left peak of each section to identify it's fringe no.
    left = peaklocs(i); %left-hand limit of current fringe(current peak)
    center = valleylocs(i); %local min at center of fringe. point at which
slope changes from negative to positive
    right = peaklocs(i+1); %right-hand limit of current fringe(next peak)
    fringeno = i-1; %fringe no. starts at 0 and iterates up in increments of
1

    delta(left:center) = lambda/(2*nl).*( fringeno +
(theta(left:center)/pi) ); %negative slope section, use negative formula
    delta(center:right) = lambda/(2*nl).*( fringeno +1 -
(theta(center:right)/pi) ); %positive slope section, use positive formula
end
if(length(peaklocs) == length(valleylocs)) %catch case of extra negative 1/2
fringe
    left = peaklocs(end); %left-hand limit of extra 1/2 fringe(last peak)
    center = valleylocs(end); %right-hand limit of extra 1/2 fringe(last
valley)
    delta(left:center) = lambda/(2*nl).*( fringeno +1 +
(theta(left:center)/pi) ); %negative slope section, use negative formula
end
if(viewplots == 1) %plot film profile if plots desired
    figure(23);
```

```
    plot(indexsize*datindex(1:peaklocs(2)), delta(1:peaklocs(2)), '-- k',
indexsize*datindex(peaklocs(2):end), delta(peaklocs(2):end), 'k')
    title('Film Thickness Profile')
    xlabel('Distance Along Profile (micrometer)')
    ylabel('Film Thickness (nanometer)')
end

%output film profile to original function call
%%%%%%%%%%%%%%%%%%%%%%%%%%%%%%%%%%%%%%%%%%%%%%%%%%%%%%%%%%%%%%%%%%%%%%%%%%%%%%%
film_profile = delta;
end
```

APPENDIX E. INTERFEROMETRY IMAGES

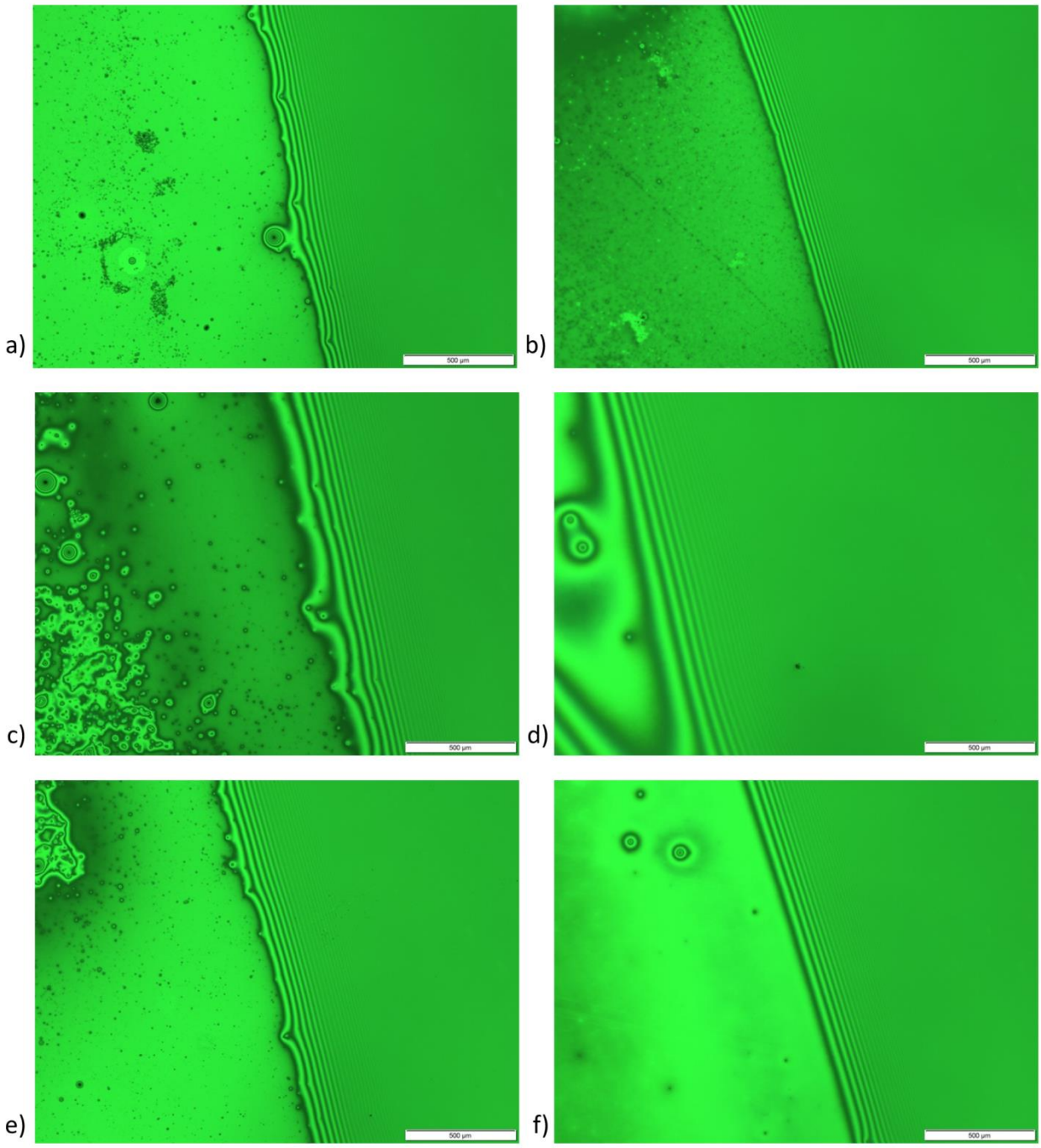

Figure 22. Interferometry images of octane on a smooth silicon wafer for apparent fill levels of a) 30%, b) 35%, c) 40%, d) 45%, e) 50%, f) 55%, g) 60%, and h) 65%.

Figure 22 continued

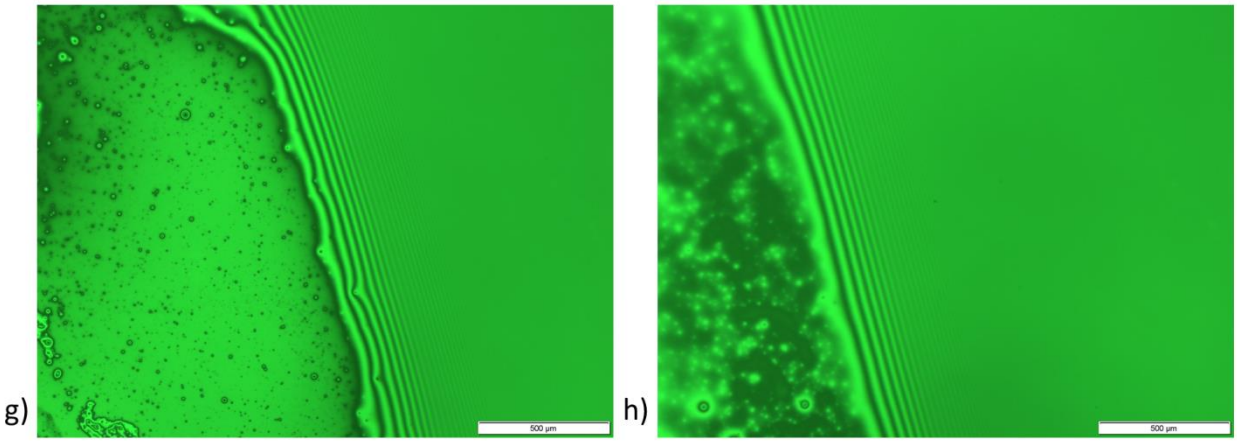

a)

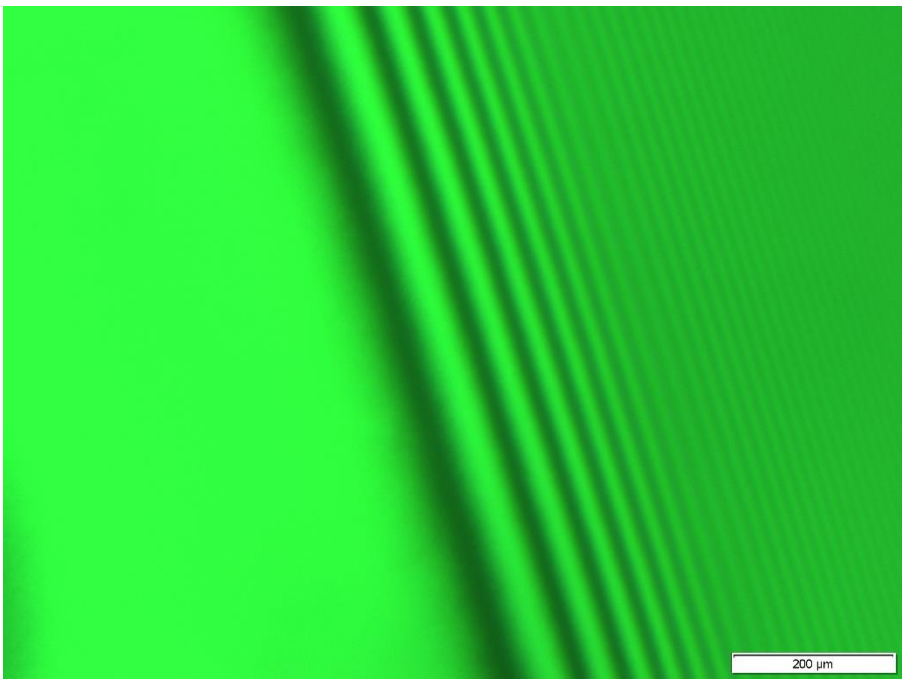

b)

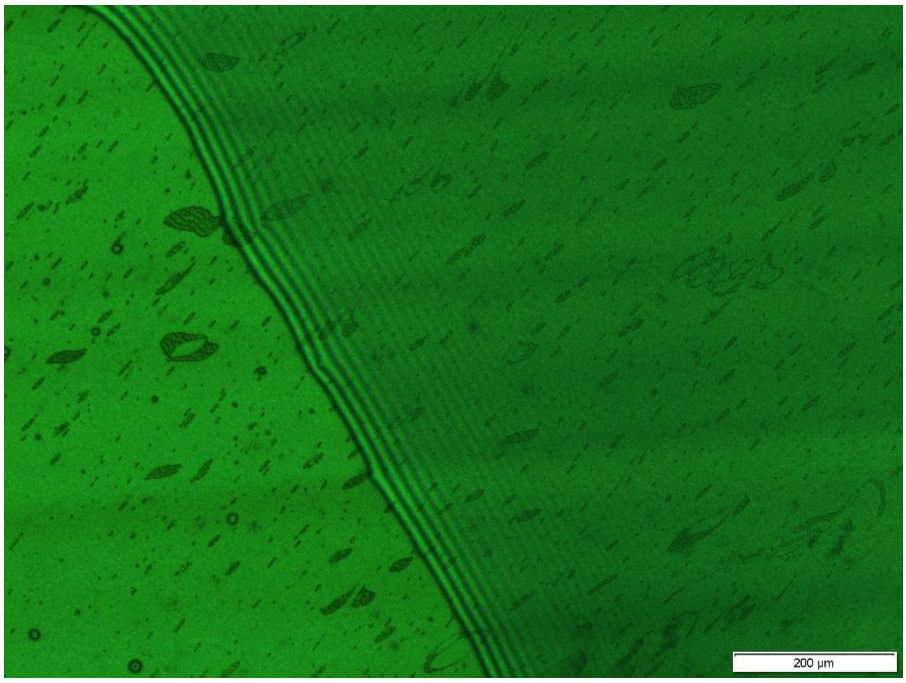

Figure 23. Interferometry fringes of octane on a) plain silicon surface and silicon surfaces with nanowires grown from Ag Catalyzed Etching with etch times of b) 20 s, c) 60 s, d) 180 s.

Figure 23 continued

c) 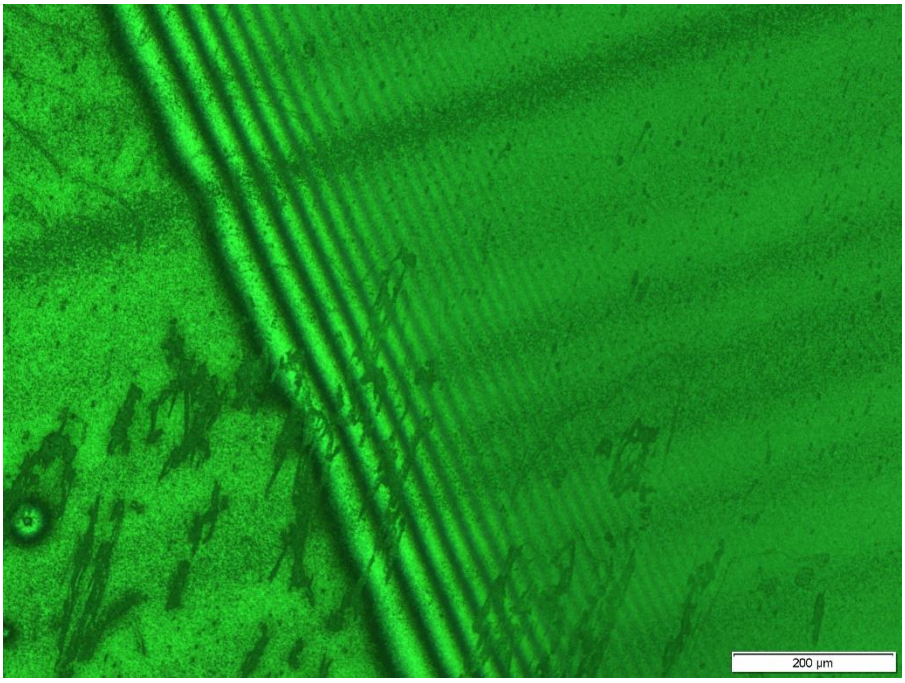

d) 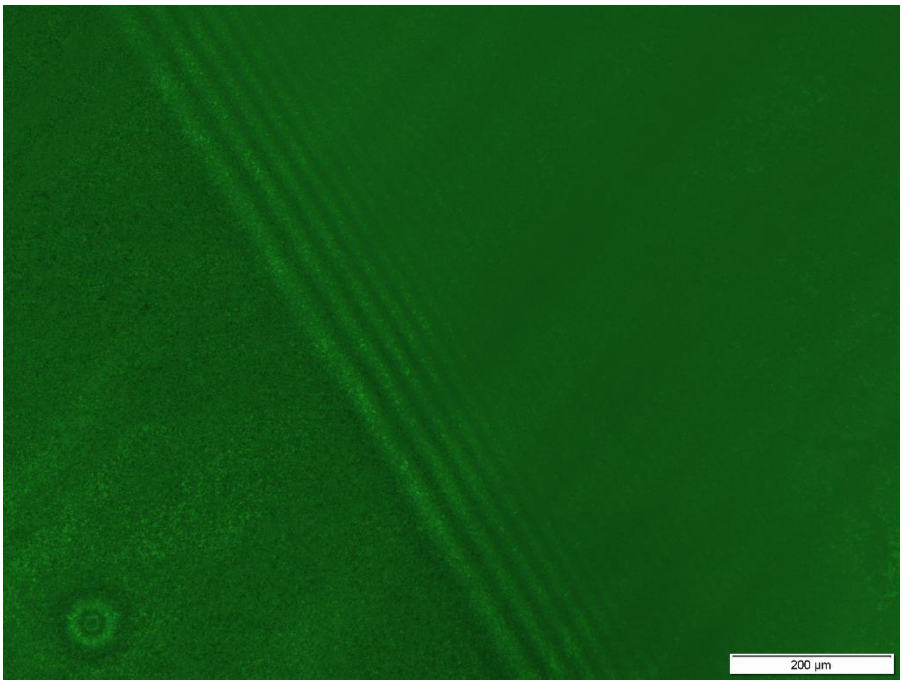

REFERENCES

[1] A. Bar-Cohen, P. Wang, and E. Rahim, “Thermal management of high heat flux nanoelectronic chips,” *Microgravity Sci. Technol.*, vol. 19, no. 3, pp. 48–52, Oct. 2007.

[2] C. G. Tua, T. Pratt, and A. I. Zaghloul, “A study of interpulse instability in gallium nitride power amplifiers in multifunction radars,” *IEEE Trans. Microw. Theory Tech.*, vol. 64, no. 11, pp. 3732–3747, Nov. 2016.

[3] R. Pastuszko and T. M. Wójcik, “Experimental investigations and a simplified model for pool boiling on micro-fins with sintered perforated foil,” *Exp. Therm. Fluid Sci.*, vol. 63, pp. 34–44, May 2015.

[4] Y.-Y. Li, Z.-H. Liu, and G.-S. Wang, “A predictive model of nucleate pool boiling on heated hydrophilic surfaces,” *Int. J. Heat Mass Transf.*, vol. 65, pp. 789–797, Oct. 2013.

[5] J. G. Truong and P. C. W. Jr, “Effects of capillary and van der Waals dispersion forces on the equilibrium profile of a wetting liquid: Theory and experiment,” *J. Chem. Phys.*, Aug. 1998.

[6] R. Argade, S. Ghosh, S. De, and S. DasGupta, “Experimental investigation of evaporation and condensation in the contact line region of a thin liquid film experiencing small thermal perturbations,” *Langmuir*, vol. 23, no. 3, pp. 1234–1241, Jan. 2007.

[7] M. S. Hanchak, M. D. Vangsness, J. S. Ervin, and L. W. Byrd, “Model and experiments of the transient evolution of a thin, evaporating liquid film,” *Int. J. Heat Mass Transf.*, vol. 92, pp. 757–765, Jan. 2016.

[8] M. S. Hanchak, M. D. Vangsness, L. W. Byrd, J. S. Ervin, and J. G. Jones, “Profile measurements of thin liquid films using reflectometry,” *Appl. Phys. Lett.*, vol. 103, no. 21, p. 211607, Nov. 2013.

[9] M. S. Hanchak, M. D. Vangsness, L. W. Byrd, and J. S. Ervin, “Thin film evaporation of n-octane on silicon: Experiments and theory,” *Int. J. Heat Mass Transf.*, vol. 75, pp. 196–206, Aug. 2014.

[10] A. Chatterjee, J. L. Plawsky, and P. C. Wayner Jr., “Disjoining pressure and capillarity in the constrained vapor bubble heat transfer system,” *Adv. Colloid Interface Sci.*, vol. 168, no. 1–2, pp. 40–49, Oct. 2011.

[11] A.-H. Liu, P. C. Wayner, and J. L. Plawsky, “Drainage of a partially wetting film: dodecane on silicon,” *Ind. Eng. Chem. Res.*, vol. 35, no. 9, pp. 2955–2963, Jan. 1996.

[12] “Image scanning ellipsometry for measuring the transient, film thickness profiles of draining liquids,” *Phys. Fluids*, vol. 6, no. 6, pp. 1963–1971, Jun. 1994.

[13] "Molecular conformation and disjoining pressure of polymeric liquid films," *J. Chem. Phys.*, vol. 94, no. 12, pp. 8420–8427, Jun. 1991.

[14] P. M. Jones *et al.*, "Measurement of disjoining pressure of Z-type perfluoropolyether lubricants on Si and SiNx surfaces," *Tribol. Int.*, vol. 38, no. 6–7, pp. 528–532, Jun. 2005.

[15] A. P. Bowles, Y.-T. Hsia, P. M. Jones, J. W. Schneider, and L. R. White, "Quasi-equilibrium AFM measurement of disjoining pressure in lubricant nano-films I: Fomblin Z03 on silica," *Langmuir*, vol. 22, no. 26, pp. 11436–11446, Dec. 2006.

[16] A. Checco, Y. Cai, O. Gang, and B. M. Ocko, "High resolution non-contact AFM imaging of liquids condensed onto chemically nanopatterned surfaces," *Ultramicroscopy*, vol. 106, no. 8–9, pp. 703–708, Jun. 2006.

[17] R. García and R. Pérez, "Dynamic atomic force microscopy methods," *Surf. Sci. Rep.*, vol. 47, no. 6–8, pp. 197–301, Sep. 2002.

[18] D. I. Driscoll, R. L. Schmitt, and W. H. Stevenson, "Thin flowing liquid film thickness measurement by laser induced fluorescence," *J. Fluids Eng.*, vol. 114, no. 1, pp. 107–112, Mar. 1992.

[19] A. E. Smart and R. A. J. Ford, "Measurement of thin liquid films by a fluorescence technique," *Wear*, vol. 29, no. 1, pp. 41–47, Jul. 1974.

[20] C. H. Hidrovo and D. P. Hart, "Emission reabsorption laser induced fluorescence (ERLIF) film thickness measurement," *Meas. Sci. Technol.*, vol. 12, no. 4, p. 467, 2001.

[21] M. Ojha, A. Chatterjee, G. Dalakos, P. C. Wayner, and J. L. Plawsky, "Role of solid surface structure on evaporative phase change from a completely wetting corner meniscus," *Phys. Fluids*, vol. 22, no. 5, p. 052101, May 2010.

[22] P. Hlubina, J. Luňáček, D. Ciprian, and R. Chlebus, "Spectral interferometry and reflectometry used to measure thin films," *Appl. Phys. B*, vol. 92, no. 2, p. 203, Jun. 2008.

[23] A.-H. Liu, P. C. Wayner, and J. L. Plawsky, "Image scanning ellipsometry for measuring nonuniform film thickness profiles," *Appl. Opt.*, vol. 33, no. 7, pp. 1223–1229, Mar. 1994.

[24] A. En Naciri, L. Broch, L. Johann, and R. Kleim, "Fixed polarizer, rotating-polarizer and fixed analyzer spectroscopic ellipsometer: accurate calibration method, effect of errors and testing," *Thin Solid Films*, vol. 406, no. 1, pp. 103–112, Mar. 2002.

[25] A. Hoang, G. Berteloot, P. Sharif-Kashani, and H. P. Kavehpour, "Dynamic measurement of microfilms and nanofilms of fluids using fluorescence microscopy," *Exp. Fluids*, vol. 52, no. 6, pp. 1657–1662, Jun. 2012.

[26] R. Patel and S. Garimella, "Technique for quantitative mapping of three-dimensional liquid-gas phase boundareis in microchannel flows," *CTRC Res. Publ.*, Jan. 2014.

[27] H. Hu, M. Chakraborty, T. P. Allred, J. A. Weibel, and S. V. Garimella, “Multiscale modeling of the three-dimensional meniscus shape of a wetting liquid film on micro-/nanostructured surfaces,” *Langmuir*, vol. 33, no. 43, pp. 12028–12037, Oct. 2017.

[28] M. Chakraborty, R. Chatterjee, U. U. Ghosh, and S. DasGupta, “Electrowetting of partially wetting thin nanofluid films,” *Langmuir*, vol. 31, no. 14, pp. 4160–4168, Apr. 2015.

[29] M. Mehran, S. Mohajerzadeh, Z. Sanaee, and Y. Abdi, “Nanograss and nanostructure formation on silicon using a modified deep reactive ion etching,” *Appl. Phys. Lett.*, vol. 96, no. 20, p. 203101, May 2010.

[30] Y. He, C. Jiang, H. Yin, J. Chen, and W. Yuan, “Superhydrophobic silicon surfaces with micro–nano hierarchical structures via deep reactive ion etching and galvanic etching,” *J. Colloid Interface Sci.*, vol. 364, no. 1, pp. 219–229, Dec. 2011.

[31] M.-C. Yang, J. Shieh, C.-C. Hsu, and T.-C. Cheng, “Well-aligned silicon nanograss fabricated by hydrogen plasma dry etching,” *Electrochem. Solid-State Lett.*, vol. 8, no. 10, pp. C131–C133, Oct. 2005.

[32] J. Shieh, S. Ravipati, F.-H. Ko, and K. (Ken) Ostrikov, “Plasma-made silicon nanograss and related nanostructures,” *J. Phys. Appl. Phys.*, vol. 44, no. 17, p. 174010, 2011.

[33] M. Y. Kim, D. S. Kim, S. K. Byeon, W. Song, and D. Lim, “Analysis of the effect of silicon with nano-size surface structure on an electrode formed using screen printing,” *J. Nanosci. Nanotechnol.*, vol. 16, no. 5, pp. 5222–5226, May 2016.

[34] S. Li *et al.*, “Structure and antireflection properties of SiNWs arrays form mc-Si wafer through Ag-catalyzed chemical etching,” *Appl. Surf. Sci.*, vol. 369, pp. 232–240, Apr. 2016.

[35] X. Chen, R. S. Patel, J. A. Weibel, and S. V. Garimella, “Coalescence-induced jumping of multiple condensate droplets on hierarchical superhydrophobic surfaces,” *Sci. Rep.*, vol. 6, p. 18649, Jan. 2016.

[36] “Inferred pressure gradient and fluid flow in a condensing sessile droplet based on the measured thickness profile,” *Phys. Fluids*, vol. 16, no. 6, pp. 1942–1955, Apr. 2004.